# Reconstruction and Evaluation of DEMs From Bistatic Tandem-X SAR in Mountainous and Coastal Areas of China

Peng Li, Zhenhong Li, *Senior Member, IEEE*, Keren Dai, Yasir Al-Husseinawi, Wanpeng Feng, and Houjie Wang

***Abstract*—TerraSAR-X add-on for Digital Elevation Measurements (TanDEM-X) mission is designed to generate 3-D images of the Earth as the first bistatic synthetic aperture radar (SAR). However, few quantitative studies of TanDEM-X digital elevation model (DEM) quality validation have been conducted specifically in China. This article presents an iterative method to generate high-resolution TanDEM-X DEMs and assesses the vertical accuracy with high-accuracy GPS observations, 1 arc second global DEMs available [Advanced Land Observing Satellite World 3-D-30 m v2.2, Advanced Spaceborne Thermal Emission and Reflection Radiometer Global Digital Elevation Model (ASTER GDEM) v3, Shuttle Radar Topography Mission (SRTM) v3.1, NASADEM, and X-band SRTM], and TanDEM-X 90 m DEM. The results demonstrate remarkable elevation quality and consistency in coastal areas with root mean square error of 1.7 m and 90% linear error (LE90) of 0.4 m, whereas 3–4 times weaker accuracies in steep mountainous areas. A positive bias of 1–2 m for an overall LE90 measure exists in the dense vegetation and steep-slope mountainous areas. TanDEM-X DEM-based SAR interferometry deformation uncertainty simulation indicates a low or even negligible topographic error contribution of 2–4 mm in mountainous areas and less than 1 mm in coastal areas. It indicates that the TanDEM-X DEM performs better than other global DEMs overall and shows a better elevation consistence with SRTM C-band DEM in the coastal area. As an excellent source of up-to-date information, the TanDEM-X DEM are expected be an advantage for understanding dynamic land use changes and improving identification and delineation of coastal lands, mountainous landslides, and earthquakes disasters.**

***Index Terms*—Coastal area, deformation monitoring, digital elevation model (DEM), GPS measurements, land cover, mountainous area, quality evaluation, robust estimation, synthetic aperture radar interferometry (InSAR), TerraSAR-X add-on for Digital Elevation Measurements (TanDEM-X).**

Manuscript received September 30, 2020; revised February 20, 2021; accepted April 13, 2021. Date of publication April 16, 2021; date of current version May 27, 2021. This work was supported in part by the Natural Science Foundation of China under Grant 41806108; in part by the National Key Research and Development Program of China under Grant 2017YFE0133500 and Grant 2016YFA0600903; in part by the Open Research Fund of State Key Laboratory of Estuarine and Coastal Research under Grant SKLEC-KF202002; in part by the State Key Laboratory of Geodesy and Earth's Dynamics, Innovation Academy for Precision Measurement Science and Technology, Chinese Academy of Sciences under Grant SKLGED2021-5-2; in part by the Sichuan Science and Technology Plan Project under Grant 19YYJC2206; in part by the U.K. NERC through the Center for the Observation and Modeling of Earthquakes, Volcanoes and Tectonics under Grant come30001; in part by the LICS Project under Grant NE/K010794/1; in part by the CEDRRIC Project under Grant NE/N012151/1; and in part by the European Space Agency through the ESA-MOST DRAGON-4&5 Projects under Grant 32244. *(Corresponding authors: Zhenhong Li; Houjie Wang.)*

Peng Li is with the Key Laboratory of Submarine Geosciences and Prospecting Technology, Institute of Estuarine and Coastal Zone, College of Marine Geosciences, Ministry of Education, Qingdao 266100, China, with the Laboratory of Marine Geology, Qingdao National Laboratory for Marine Science and Technology, Qingdao 266237, China, and also with the State Key Laboratory of Estuarine and Coastal Research, East China Normal University, Shanghai 200241, China (e-mail: pengli@ouc.edu.cn).

Zhenhong Li is with the Institute of Estuarine and Coastal Zone, College of Marine Geosciences, Ocean University of China, Qingdao 266100, China, and also with the College of Geological Engineering and Geomatics, Chang'an University, Xi'an 710054, China (e-mail: zhenhong.li@newcastle.ac.uk).

Keren Dai is with the College of Earth Sciences and the State Key Laboratory of Geohazard Prevention and Geoenvironment Protection, Chengdu University of Technology, Chengdu 610059, China (e-mail: daikeren17@cdut.edu.cn).

Yasir Al-Husseinawi is with the Ministry of Water Resources, State Commission of Survey, Baghdad 734-7-13, Iraq (e-mail: bdysrb@gmail.com).

Wanpeng Feng is with the Guangdong Provincial Key Laboratory of Geodynamics and Geohazards, School of Earth Sciences and Engineering, Sun Yat-Sen University, Guangzhou 5100275, China, and also with the Southern Marine Science and Engineering Guangdong Laboratory, Zhuhai 519080, China (e-mail: fengwp5@mail.sysu.edu.cn).

Houjie Wang is with the Key Laboratory of Submarine Geosciences and Prospecting Technology, Institute of Estuarine and Coastal Zone, College of Marine Geosciences, Ministry of Education, Ocean University of China, Qingdao 266237, China, and also with the Laboratory of Marine Geology, Qingdao National Laboratory for Marine Science and Technology, Qingdao 266237, China (e-mail: hjwang@ouc.edu.cn).

Digital Object Identifier 10.1109/JSTARS.2021.3073782

## I. Introduction

TOPOGRAPHY is a key parameter that influences many of the fundamental geophysical processes involved in Earth sciences and environmental research (e.g., geology, glaciology, oceanography, meteorology, and hydrology), as well as geolocation-based services, such as land use, vegetation monitoring, urban and infrastructure planning, cartography, navigation, logistics, crisis management, defense and security environment changes [1]–[11].

Researchers investigating global changes have an increasing demand for up-to-date, high-resolution, high-accuracy digital elevation model (DEM) data [12]. Over the last two decades, freely available global DEMs with spatial resolution of up to 1 arc second have played a crucial role in terms of alternative topographic sources. For example, Shuttle Radar Topography Mission (SRTM) DEM from C-band and X-band synthetic aperture radar interferometry (InSAR) technique, Advanced Spaceborne Thermal Emission and Reflection Radiometer Global Digital Elevation Model (ASTER GDEM) and Advanced Land Observing Satellite (ALOS) World 3-D-30 m (AW3D30) from optical stereo images have been widely used in the world [1], [6], [13]–[20].

As the world's first bistatic synthetic aperture radar (SAR) mission to be formed with two almost identical satellites flying in a closely controlled formation with typical distances between 250 and 500 m, TerraSAR-X add-on for Digital Elevation Measurements (TanDEM-X) mission has been designed to generate consistent 3-D images of the Earth with homogeneous quality and unprecedented accuracy [21]. The TanDEM-X mission has measured the entire land surface of the Earth that is 150 million square kilometers several times completely since 2010 [22]. With TerraSAR-X and TanDEM-X mission flying in close formation and transmitting pulses from the antenna of only one of the satellites and by receiving the backscattered signals simultaneously with both, TanDEM-X DEM can be generated from single-pass cross-track bistatic InSAR technique, which is less affected by temporal decorrelation and atmospheric disturbances. In addition to the high horizontal resolution and vertical accuracy, the consistently homogeneous DEM created with the TanDEM-X and TerraSAR-X satellites is the basis for a uniform map material worldwide and beneficial for the dynamic monitoring of the Earth's surface, e.g., height changes in glaciers, permafrost regions, forests, agricultural activities, and infrastructure. The specified quality of the final TanDEM-X DEM at a large scale would be of considerable interests for the scientific and commercial users [23].

The official final global TanDEM-X DEM products with 0.4 arc second (approximately 12 m at the equator) horizontal grid spacing benefit from mapping all land surfaces at least twice and difficult terrain even up to eight times since 2010 [21]–[23]. Since October 8, 2018, the German Aerospace Center (DLR) has released the 3-arc second (90 m) version at no charge for scientific use, which is derived from 12 m global products with last update on December 5, 2019. The 12 m TanDEM-X DEM have a specified 10 m absolute vertical accuracy with regard to 90% linear error (LE90) and 2 m relative accuracy with respect to 4 m for areas with slopes larger than 20% with regard to 90% linear point-to-point error [21]. Its commercial version WorldDEM$^{\rm TM}$ is released from Airbus Defense and Space in different versions on October 31, 2018, e.g., with geoid elevations or further value-additions.

Numerous articles have been published concerning the quality of TanDEM-X elevation data on different releases including TanDEM DEMs generated from Coregistered Single look Slant range Complex (CoSSC) SAR data, intermediate digital elevation models (IDEM), commercial WorldDEM$^{\rm TM}$, and 90 and 12 m TanDEM-X global products covering miscellaneous areas [1], [2], [4]–[8], [19], [22]–[29]. The TanDEM-X DEMs with resolution of 12 m or higher show an outstanding performance in most of the studies mentioned above. For example, Avtar, Yunus, Kraines, and Yamamuro [8] estimated the vertical accuracy (3.20 m) of root mean square error (RMSE) of TanDEM-X over Tokyo coastal area from the CoSSC data with 2 m LiDAR as reference. Baade and Schmullius [24] validated the absolute vertical height error (RMSE = 1.03 m, LE90 = 1.5 m) of TanDEM IDEM with real-time kinematic (RTK) global positioning system (GPS) based ground survey points in the open terrain area over the Kruger National Park in South Africa and provided evidence in the sensitivity to canopy cover. Becek, Koppe, and Kutoğlu [27] presented on the vertical accuracy assessment (RMSE = 1.39 m) of the WorldDEM$^{\rm TM}$ with runway centerlines of airports worldwide. Lee and Ryu [28] generated intertidal zone TanDEM-X DEMs on the west coast of Korean Peninsula with 5–7 m spatial resolutions and validated them against GPS RTK measurements with an RMSE of 0.20 m. Zhang, Gann, Ross, Robertson, Sarmiento, Santana, Rhome, and Fritz [29] and González-Moradas and Viveen [6] reported an almost identical vertical accuracy (RMSE = 1.7 m) for 12 m TanDEM-X DEM in the two different areas, that is, Caribbean and Peruvian Andes, respectively. The official validation report with GPS data from Wessel, Huber, Wohlfart, Marschalk, Kosmann, and Roth [23] proved the well-performed TanDEM-X 12m DEM with an RMSE of less than 1.4 m. Nonetheless, Altunel [25] showed that TanDEM-X 90m (TDX90) DEM are overestimated in broken to treacherous terrain in comparison to both 30 and 90 m SRTM DEMs. Besides, Hawker, Neal, and Bates [2] revealed that vertical error of TDX90 DEM is lower for all landcover categories except for short vegetation and tree covered areas.

Since the quality of DEMs varies spatially in a regional level, TanDEM-X DEM should be assessed quantitatively and used carefully. However, few validation studies have focused specifically on China as a result of the limited availability of the TanDEM-X DEM generated from the CoSSC SAR data as well as intermediate or final version. In this article, we generate high-resolution TanDEM-X DEMs from the CoSSC scenes in the mountainous and coastal areas of China. Then, we use high-precision GPS measurements and 1 arc second global DEMs available to estimate the vertical accuracy by means of both classical and robust statistical methods and analyze the correlation between height differences and slope derivatives. Furthermore, the results are separated into different land cover classes from the 10 m global land cover dataset to investigate the spatial patterns of the TanDEM-X DEM error. Finally, we simulate the topographic error contribution to Sentinel-1 InSAR deformation uncertainty.

## II. Datasets and Methods

### A. TanDEM-X DEM

All the TanDEM-X DEMs over the study areas were derived from the acquired CoSSC data in StripMap mode with ENVI SARScape. Table I presents the detailed information for all CoSSC data in three study areas. Since the CoSSC data are already coregistered, the processing flowchart for DEM generation illustrated on Fig. 1 consists of a two rounds of iteration, each of which includes interferogram generation, phase removal, phase unwrapping, absolute phase calibration, and geocoding [30]–[32]. The detailed steps are as follows.

1) The grid size of 12 m as well as suggested looks of 5∗5 are first set before generating an interferogram from the primary and secondary COSSC data.
2) The National Aeronautics and Space Administration (NASA) Version 3.0 Global 1 arc second Shuttle Radar Topography Mission (SRTMGL1) data with no elevation

TABLE I
DETAILED INFORMATION OF THE TANDEM-X COSSC DATA USED IN THE STUDY

| Study Area | Geographical Coverage | Length/Width | Acquisition Date | Baseline | HOA | Orbit Cycle/Orbit Number | Orbit Direction |
|---|---|---|---|---|---|---|---|
| WC | [103-104°E, 31-32°N] | [12957, 11212] | 2012/12/28 | 311.3m | 23.3 | 184/30726/165 | Descending |
| TG | [110-112°E, 30-32°N] | [8895, 8410] | 2011/09/21 | 141.0m | 43.3 | 142/23674/127 | Ascending |
| QD | [119-121°E, 35-37°N] | [12375, 13161] | 2012/09/04 | 208.8m | -32.8 | 174/28972/081 | Ascending |

Note: WC, Wenchuan; TG, Three Gorges; QD, Qingdao; HOA, Height of Ambiguity.

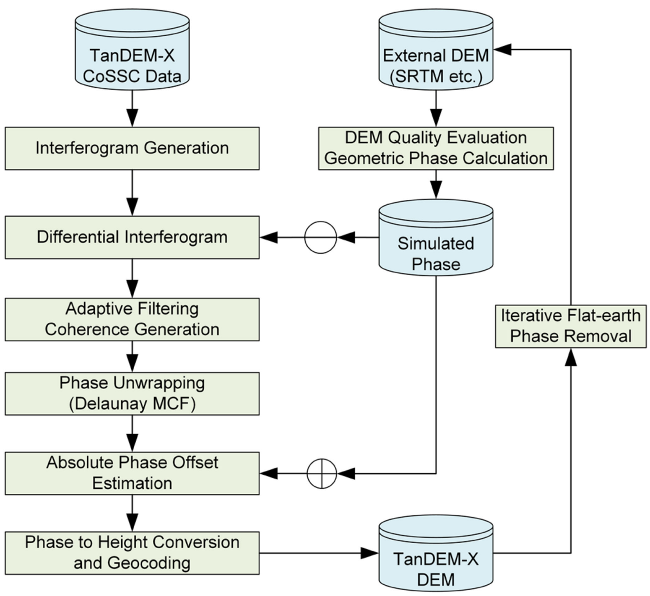


Fig. 1. Flowchart of high-resolution TanDEM-X DEM generation in this study.

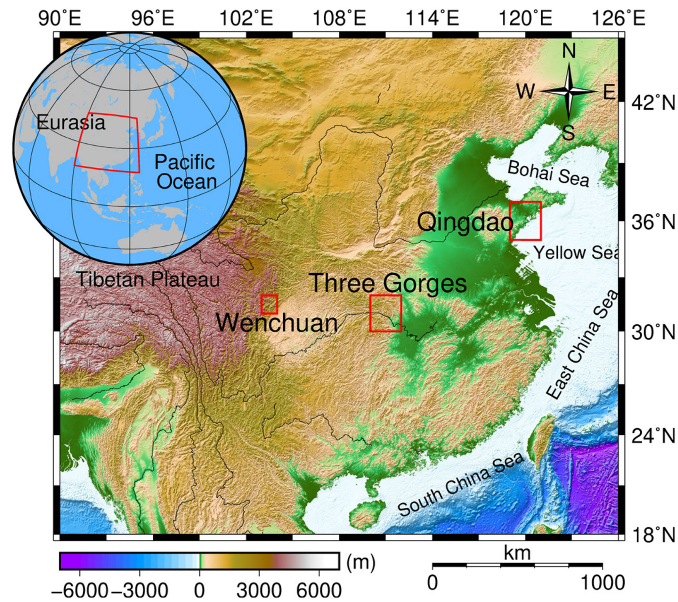


Fig. 2. Locations of the three study areas (Wenchuan mountainous area, Three Gorges area, and Qingdao coastal area) over China denoted as red box on a shaded relief map derived from ETOPO1 topography.

voids are used to simulate the topographic phase contribution [11]. To be consistent with each other in the following comparison, the SRTMGL1 and other global DEMs with orthometric elevations regarding to the Earth Gravitational Model 1996 geopotential model should be first converted to the World Geodetic System (WGS84) ellipsoidal elevations [33], [34]. Differential interferograms are derived with removal of the topography simulation from the SRTMGL1.

3) The adaptive filtering of the flattened interferogram enables to generate an output product with reduced phase noise [35], [36]. The coherence values are used to set the filter window size, while the mean intensity difference among adjacent pixels is used to identify a stationary area. A coherence threshold of 0.4 is set to mask out the incoherent region for coastal plain area, while 0.6 for steep mountainous area.
4) Delaunay Minimum Cost Flow method is employed for phase unwrapping, which is especially useful for solving the $2\pi$ ambiguity of the differential interferograms when there are several areas of low coherence (e.g., water bodies and densely vegetated areas) distributed throughout the image [37].
5) The real topographic phase is retrieved by adding back simulated topography phase into the unwrapped differential phase [8].
6) Phase to height conversion and geocoding are conducted to derive the DEM heights with WGS84 geographic coordinates.
7) For the iteration section, the grid size of 5 m and suggested looks of $2*2$ in range (4.1 m) and azimuth (4.0 m) are set for the generation of a new TanDEM-X DEM. The TanDEM-X 12 m DEM obtained above is adopted to remove the topography contribution, while other parameter settings can remain the same. For the sake of simplicity, we use the abbreviation of TDX4 to distinguish it from the TDX90 thereinafter.

## B. GPS Data

As shown in Fig. 2, there are three study areas used for the accuracy evaluation of TanDEM-X DEMs, including two mountainous areas in Wenchuan and Three Gorges as well as one coastal area in Qingdao. As a result of the distinctly different geographical locations, spatial independence and complex topography can be assured, which is fairly advantageous to this article. All ground control points (GCPs) in Wenchuan and Qingdao area used for the absolute vertical accuracy comparison of TanDEM-X DEM were derived from GPS static and RTK mode observations carried out in the last two years, defined in the WGS84 datum with a general accuracy of approximately

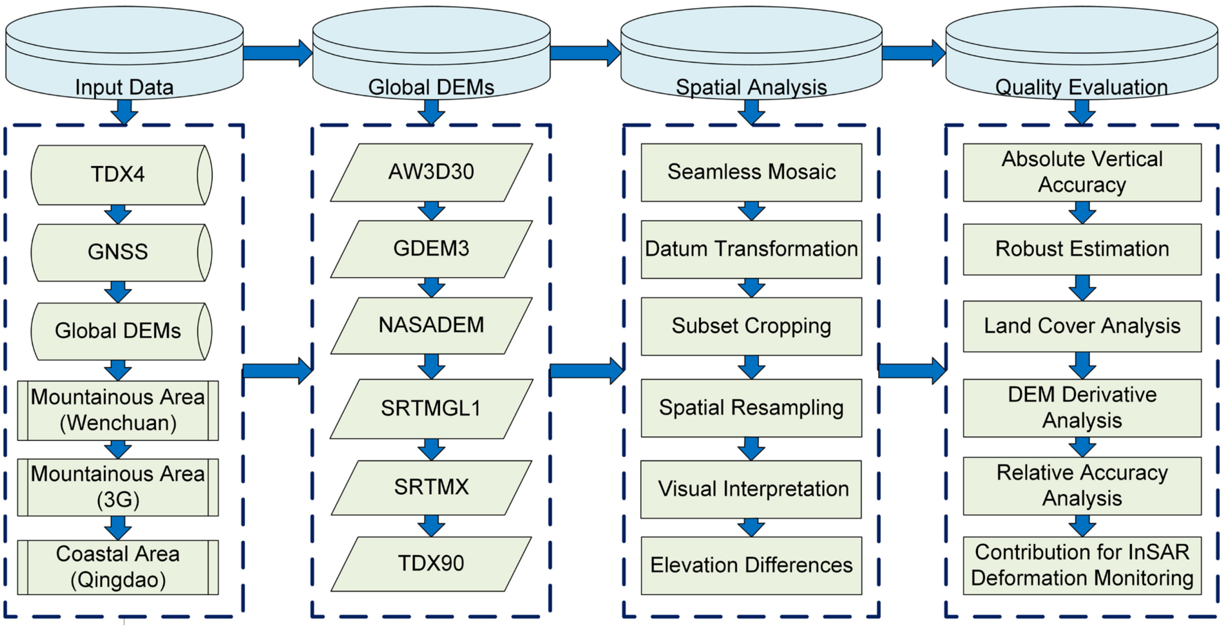


Fig. 3. Flowchart of the TanDEM-X DEM quality evaluation in this study.

TABLE II
DEM Product Specifications in This Study

| Global DEM | Methodology | Pixel Spacing | Tile Size | Vertical Datum | Void Value | Byte Order | Vertical Accuracy | Exposure | References |
|---|---|---|---|---|---|---|---|---|---|
| AW3D30 | PRISM Stereo | 1″ | 1° | EGM96 | -9999 | LE | 5m (RMSE) | 2006-2011 | [20] |
| GDEM3 | ASTER Stereo | 1″ | 1° | EGM96 | -9999 | LE | 17m (LE95) | 2000-2015 | [38] |
| NASADEM | C-band InSAR | 1″ | 1° | EGM96 | -32768 | BE | 16m (LE90) | 2000 | [39] |
| SRTMGL1 | C-band InSAR | 1″ | 1° | EGM96 | -32768 | BE | 16m (LE90) | 2000 | [13] |
| SRTMX | X-band InSAR | 1″ | 15' | WGS84 | -32767 | BE | 16m (LE90) | 2000 | [14] |
| TDX90 | X-band InSAR | 3″ | 1° | WGS84 | -32767.0 | LE | 10m (LE90) | 2006-2015 | [23] |
| TDX4 | X-band InSAR | 0.15″ | — | WGS84 | NAN | LE | — | 2011-2012 | — |

Note that:
1) AW3D30 is the ALOS World 3-D-30m v2.2, GDEM3 is the ASTER GDEM v3 that is a product of METI and NASA, NASADEM is a modernization of the DEM and associated products generated from the SRTM data freely available through the LP DAAC, SRTMGL1 is the C-band InSAR-derived NASA v3.0 SRTM (SRTM Plus), SRTMX is the X-band InSAR-derived SRTM DEM, and TDX4 is the X-band InSAR-derived TanDEM-X DEM at the resolution of approximately 4–5 m.
2) LE and BE stand for little-endian and big-endian byte orders, respectively.
3) LE95 and LE90 expressed as linear errors at the 95% and 90% confidence levels, respectively.

5–10 cm. Ground-truth datasets in the Three Gorges region were all derived from GPS static observation benchmarks performed in April and May 2004 with a high accuracy at the centimeter level. Fig. 4 presents a first impression of the spatial distribution of GPS GCPs in each study area. All the GPS data have been converted to WGS84 ellipsoidal elevations for comparison with DEM heights.

### C. Global DEMs

We use five different freely available 1 arc second global DEMs and 3 arc second TanDEM-X DEMs for intercomparisons with high-resolution TanDEM-X DEM as illustrated in Fig. 3. Table II shows the product specification information on all the DEMs used in this article.

*1) AW3D30 DEM v2.2:* As a free 30 m resolution version of AW3D, AW3D30 v1.0 global products were released in May 2016. This dataset is a global digital surface model (DSM) with horizontal resolution of approximately 30 m by the Panchromatic Remote-sensing Instrument for Stereo Mapping (PRISM) on board the ALOS that can be freely available at Japan Aerospace Exploration Agency Earth Observation Research Center.[1] Version 2.2 was released in April 2019 as an improved version of the northern region over 60° north with no-data or low-quality areas filled in with version 1.1 released in March 2017 and 2.1 released in April 2018, as well as updating of coastline [20].

*2) ASTER GDEM v3:* On August 6, 2019, the Ministry of Economy, Trade, and Industry of Japan and the United States NASA jointly announced the release of the ASTER GDEM v3 (hereafter named GDEM3) and the ASTER Water Body Dataset (ASTWBD). The new version datasets are derived from 1.88 million Level 1A Terra ASTER scenes acquired between March 1, 2000 and November 30, 2013, which can be downloaded

[1] [Online]. Available: https://www.eorc.jaxa.jp/ALOS/en/aw3d30/data/index.htm

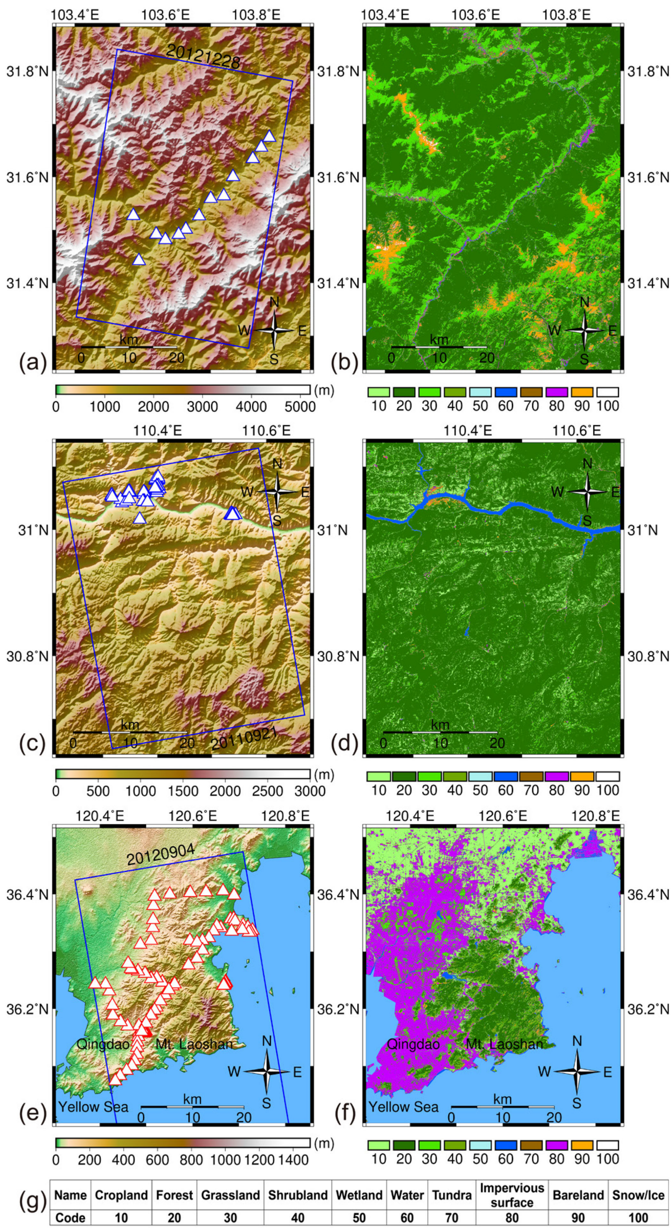


Fig. 4. Shaded relief map and land cover of the Wenchuan area (a, b), Three Gorges area (c, d), and Qingdao coastal area (e, f). Land cover class name and code are derived from classification system of FROM-GLC10 (g). Locations of GPS points are denoted by triangles filled with white color, while TanDEM-X SAR data coverage are represented by blue rectangles. Topography and land cover datasets are derived from 30 m SRTMGL1 and 10 m FROM-GLC10, respectively. The explicit definition of the land cover class can be available at the official website (http://data.ess.tsinghua.edu.cn/).

directly free of charge, e.g., via NASA Earthdata.[2] Version 3 provides improved spatial resolution, increased horizontal and vertical accuracy by adding additional stereo-pairs, improving coverage and reducing the occurrence of artifacts (e.g., cloud coverage) with refined production algorithm and other existing reference DEMs [38]. Besides, the near global raster by-product ASTWBD identifies and corrects all water bodies as ocean, river, or lake.

*3) NASADEM:* On February 13, 2020, the NASA Land Processes Distributed Active Archive Center (LP DAAC) announced the 1 arc second NASADEM products freely available, e.g., at NASA Earthdata Search. As a modernization of the SRTM DEM, the original SRTM raw signal radar data has been reprocessed with improved algorithms (e.g., phase unwrapping and height error correction). Beyond that, incorporating data for control primarily derived from the Ice, Cloud, and Land Elevation Satellite as well as ASTER GDEM (v3 and v2) and a variety of sources (e.g., ALOS PRISM) for void and artifact reduction are also considered, which was unavailable during the original SRTM processing [39].

*4) SRTMGL1:* The NASA LP DAAC released the NASA SRTMGL1 dataset collection (also known colloquially as SRTM Plus) on November 20, 2014 that can be freely available, e.g., at NASA Earthdata Search, or United States Geological Survey EarthExplorer. This version of the SRTM DEM has eliminated all voids, edited the water mask, and improved the topographic representation of shorelines with filling primarily from ASTER GDEM v2 as well as other existing DEM sources [13].

*5) SRTM X-SAR DEM:* As a precursor for the TanDEM-X mission, the SRTM X-SAR (hereafter named SRTMX) DEM was generated from X-band interferometric SAR data acquired during the Space Shuttle Endeavor acquiring data conducted jointly between the DLR, Italian Space Agency, and NASA Jet Propulsion Laboratory, in 2000 [40]. In December 2010, this dataset was accessible at no cost to the scientific community in the DLR Earth observation data catalog, e.g., via the EOWEB Geoportal.[3] Not so continuous as the coverage of the C-band SRTM DEMs is, SRTMX DEMs provides crisscrossing image strips with diamond-shaped areas of no data on account of the higher precision and hence narrow swath width of the X-SAR instrument [14].

*6) TanDEM-X 90 m DEM:* On October 8, 2018, the TDX90 was released for scientific use and is now freely available as a global dataset at DLR Earth Observation Center.[4] The global TanDEM-X data acquisition with a typical baseline of 120 to 500 m was completed in January 2015 and production of the global DEM was completed in September 2016. As a product derived from the global DEM with a 0.4 arc second (12 m) posting, the TDX90 DEM has a reduced pixel spacing of 3 arc second, corresponding to approximately 90 m at the equator [22], [23].

## *D. Methods*

Fig. 3 shows the main working flowchart of TanDEM-X DEM quality evaluation in this article. First, we need to prepare all the TanDEM-X DEMs, GPS field measurements, and global DEMs in each study area. Second, fundamental spatial analysis procedures for different DEMs are carried out with ENVI platform and interactive data language programming, including seamless mosaic, datum conversion, subset cropping, spatial resampling, visual interpretation, and elevation difference calculation and statistics. Third, detailed quality assessment comprises absolute

[2][Online]. Available: https://search.earthdata.nasa.gov/search

[3][Online]. Available: https://geoservice.dlr.de/egp/

[4][Online]. Available: https://download.geoservice.dlr.de/TDM90/

vertical accuracy, robust statistics, land cover analysis, DEM derivative (e.g., slope) analysis, relative accuracy analysis, and simulation of contribution for InSAR deformation analysis.

Considering both systematic and random errors introduced with data generation process, RMSE is a widely used measure of conformity between actual values and estimates [18], [41]. Besides, mean error (ME) and standard deviation (STD) are also used to represent the DEM errors in the case of the accuracy of reference measurements (e.g., GPS points) better than two orders of magnitude. Assuming a normal distribution, we use the following formulas to express ME, STD, and RMSE to assess the elevation errors:

$$\mathrm{ME} = \hat{\mu} = \frac{1}{N}\sum_{i=1}^{N}(H_i - H_{\mathrm{ref}}) = \frac{1}{N}\sum_{i=1}^{N}\Delta h_i \tag{1}$$

$$\mathrm{STD} = \hat{\sigma} = \sqrt{\frac{1}{N-1}\sum_{i=1}^{N}(\Delta h_i - \hat{\mu})^2} \tag{2}$$

$$\mathrm{RMS} = \sqrt{\frac{1}{N}\sum_{i=1}^{N}\Delta h_i^2} \tag{3}$$

where $H$ denotes the height and $N$ is the number of samples.

As a result of, e.g., interpolation, filtering, layover, shadow, and phase unwrapping errors in nonopen terrain, a normal distribution of DEM errors is seldom for InSAR or digital photogrammetry derived DEMs. We use both graphical and statistical methods for evaluating normality, that is, histograms and quantile–quantile (Q-Q) plots for intuitive visual inspection, as well as skewness and kurtosis measures of the error distribution. In statistics, skewness is a measure of the asymmetry of the probability distribution of a random variable about its mean, while kurtosis is defined as the degree to which a statistical frequency curve is peaked. However, sample size would have a big impact on the skewness and kurtosis results and quantile approach [42]. 3∗RMSE or $3*\sigma$ as the threshold are not used for the outlier detection as suggested by Höhle and Höhle [42] that not all of the outliers can be detected in this way and the DEM accuracy evaluation would be inaccurate or wrong.

Nonparametric estimators for robust accuracy measures have been proved to be resistant to outliers without having to assume a symmetric distribution [23], [42]. Furthermore, median (50% quantile), the median absolute deviation, the normalized median (NMAD), and the absolute deviation at the 90% quantile (LE90) in the following suited for non-normal error distributions are applied for the assessment of DEM accuracy. Although this rarely happens in the case of normal error distribution, NMAD regarded as an estimate for the STD of heavy tail distributions equals to STD, and LE90 is identical to 1.65∗STD [23]

$$\hat{Q}_{\Delta h}(0.5) = m_{\Delta h} \tag{4}$$

$$\mathrm{MAD} = \mathrm{median}_j\left(|\Delta h_j - m_{\Delta h}|\right) \tag{5}$$

$$\mathrm{NMAD} = 1.4826 \times \mathrm{median}_j\left(|\Delta h_j - m_{\Delta h}|\right) \tag{6}$$

$$\mathrm{LE90} = \hat{Q}_{|\Delta h|}(0.9). \tag{7}$$

## III. Absolute Vertical Accuracy Validation

As shown in Fig. 3, there are three test sites with different topography features used for the accuracy validation of TanDEM-X DEM, that is, the Three Gorges area, Wenchuan area, and Qingdao area. This choice is partly because of extensive anthropogenic activities from densely populated urban and rural areas that changes the land cover and land use, e.g., groundwater withdrawal, hydraulic engineering, and farming. In addition, these areas are prone to be exposed to geological hazards, e.g., landslides, earthquakes, land subsidence, and storm surge flooding, attributed to the special geographical environment, e.g., steep slope terrain, tectonic driving forces, and sea level rise [43].

Bilinear approach was employed to compare the difference between GPS and DEM heights, where positive or negative value means the DEM is higher or lower than the reference elevation, respectively. As a robust quality measure, median value of the elevation differences is less sensitive to outliers in the data than the ME, which demonstrates a systematic shift of the DEM that and provides a better distributional summary for skew distributions [23], [42]. Fig. 4 presents shaded relief map and land cover as well as spatial distribution of the GPS points. Histograms, Q-Q plots, Box–Whisker plots, and scatterplots with absolute vertical accuracy statistics of the TDX4 are shown in Figs. 5 and 6. Table III shows details of the GPS number and absolute DEM vertical accuracy from three study areas.

### A. Mountainous Area: Wenchuan

As shown in Figs. 2 and 4(a) and (b), this area located in the eastern Qinghai–Tibet Plateau is covered with medium and high vegetation where the Long–Men–Shan fault zone crosses the study area with the strike direction about N40°E and earthquakes frequently occurred in the adjacent area historically. As is a region with one of the steepest slope gradient mountainous zones in the world, a devastating Mw7.9 Wenchuan earthquake of May 12, 2008 in Sichuan Province, China, has triggered more than 56 000 landslides [44], [45]. It is ideal for examining the relationships between landsliding and orogen evolution due to its large magnitude, steep regional topography, and widespread occurrence of coseismic landslides [45]–[48].

Due to full of high and steep slopes in most Wenchuan mountainous areas, it is extremely challenging to conduct large-scale rapid GPS measurements. A total of 13 GCPs are obtained with static observation mode for at least half hour in each station along the main road, but two points just fall into the incoherent area. As can be seen in Fig. 5(a) and Table III, the ME (5.1 m) of TanDEM-X DEM is roughly equal to median error. Its NMAD (6 m) is lower than that of rms (8.8 m) and STD (7.5 m), whereas the lowest for all global DEMs. As a whole, all DSMs have a positive mean bias due to probably affected by vegetation land cover, while outliers intuitively exist for all InSAR derived DEMs, especially for TDX90 [Fig. 5(c)].

As a measure of symmetry, or more precisely, the lack of symmetry, skewness of 1.09 means the distribution is highly right-skewed [Fig. 5(a)]. As the parameter of relative sharpness of the peak of the probability distribution curve, kurtosis of 0.97 indicates the peak of the frequency distribution curve and

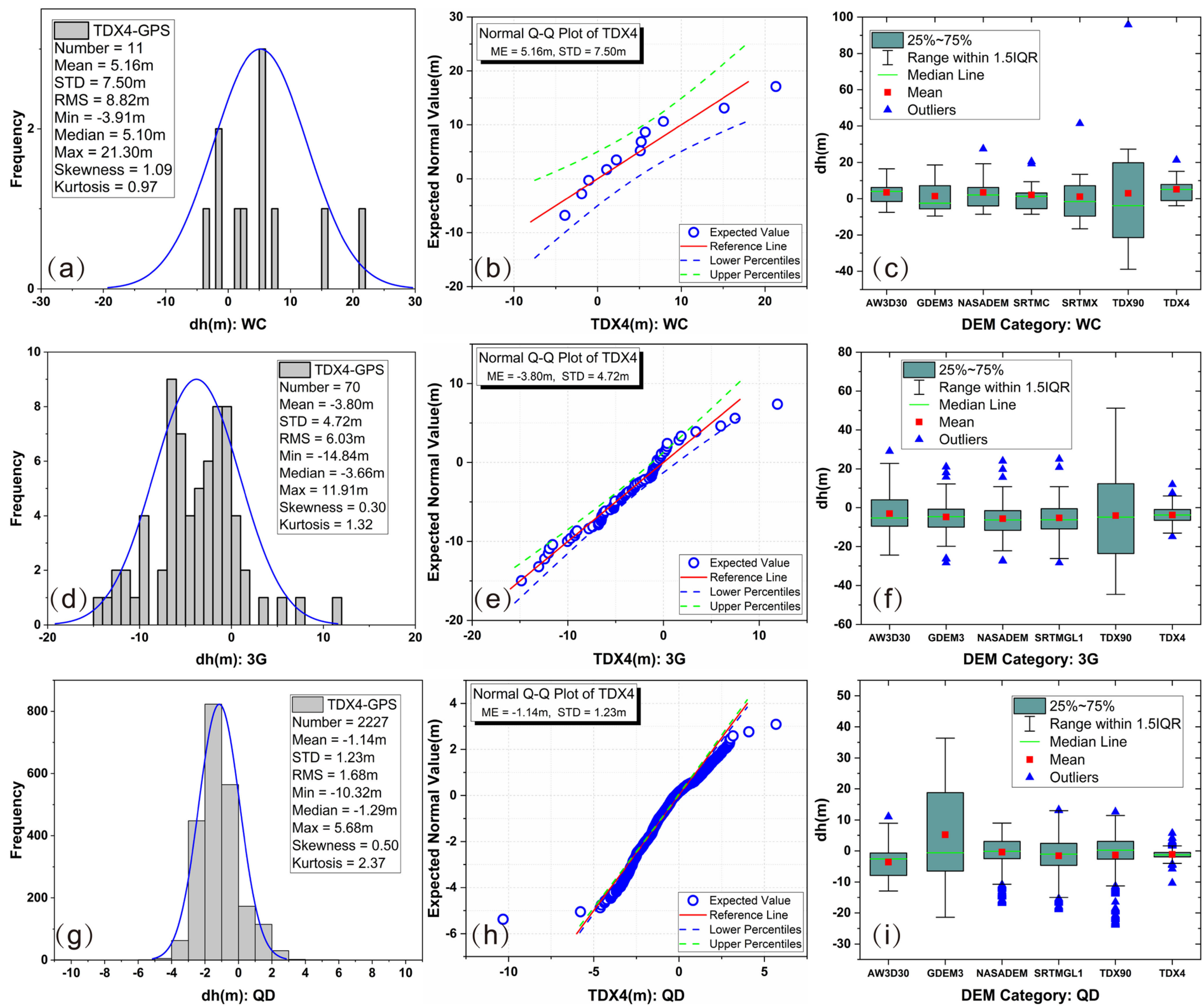


Fig. 5. Histograms, Q-Q plots, and Box–Whisker plots with absolute vertical accuracy statistics of the TDX4 and all global DEMs for the three study areas.

measures the tail or outlier of the distribution [Fig. 5(a)]. As a nonparametric approach, normal Q-Q plot is used to find out if two sets of data come from the same distribution. If the two datasets come from a common distribution, the points will fall on that reference line $y = x$. A thin-tailed distribution will form a Q-Q plot with a very less or negligible deviation at the ends thus making it a perfect fit for the normal distribution [Fig. 5(b)]. Note that when the measurement points are pretty less in this case, the Q-Q plot does not perform very precisely and it fails to give a conclusive answer.

### B. Mountainous Area: Three Gorges

In Figs. 3 and 4(c) and (d), the longest river, that is the Yangtze River in China, flows through the world famous Three Gorges Reservoir Region with full of steep mountains. Vegetation cover is dominated by subtropical evergreen broad-leaved forests vegetation as well as cropland. The Three Gorges were formed by severe incision along narrow fault zones in response to Quaternary uplift of massive limestone mountains at the lower Paleozoic and Mesozoic age [49]. Steep slopes develop extensively on easily erodible materials and the attitude of strata with respect to slope angle and aspect has a great impact on slope instability, leading to frequent landslides in this area [50]–[54].

There are 70 GPS measurements ever collected for deformation monitoring of landslides in Badong and Zigui counties, mainly located on the banks of the Yangtze River and uneven distributed due to dense vegetation and steep terrain [Fig. 4(c)]. Table III shows that TanDEM-X DEM has almost equal mean and median negative elevation biases of −3.8 m compared to GPS, while NMAD value (4.2 m) is a bit lower than that of rms (6.0 m) and STD (4.7 m) and also among the lowest for all global DEMs. Negative mean and median errors of 3–5 m exist in all DEMs, but TanDEM-X DEM performs best in terms of rms, STD, and LE90.

Fig. 5(d) shows the distribution is approximately symmetric with a skewness of 0.3, while a kurtosis of 1.32 indicates heavy tails on either side with large outliers in Fig. 5(e). Outliers can also be seen from Fig. 5(f) in most global DEMs except for

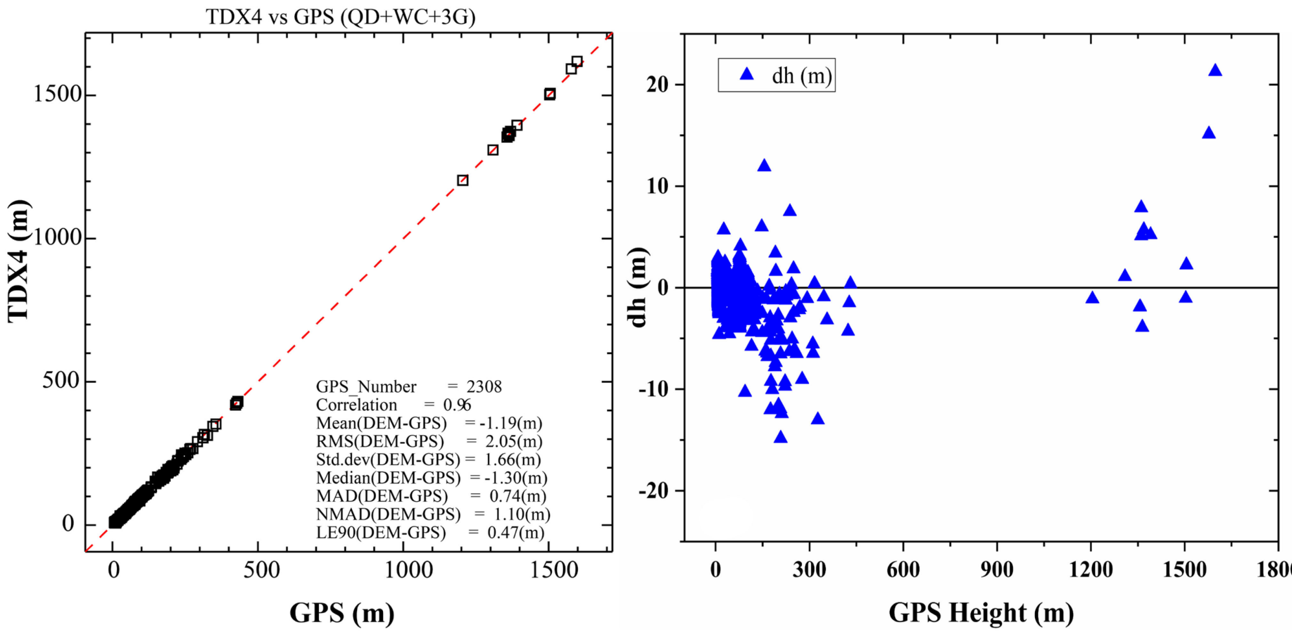


(a) (b)

Fig. 6. (a) Scatterplots of TDX4 vs. GPS. Red dashed line indicates the perfect fit. (b) Elevation differences distribution of the TDX4-GPS using all the GPS points over all of the three study areas. Corresponding GPS elevation is shown in the horizontal axis.

TABLE III
ABSOLUTE VERTICAL DEM ACCURACY IN THE STUDY AREAS

| Area | DEM-GPS | GPS No. | Corr. | Min (m) | Max (m) | ME (m) | STD (m) | RMS (m) | Median (m) | MAD (m) | NMAD (m) | LE90 (m) |
|---|---|---|---|---|---|---|---|---|---|---|---|---|
| WC | AW3D30 | 13 | 0.98 | -7.51 | 16.47 | 3.48 | 6.56 | 7.20 | 4.03 | 4.24 | 6.29 | 10.40 |
| | GDEM3 | 13 | 0.96 | -9.56 | 18.60 | 1.41 | 8.40 | 8.20 | 1.41 | 6.78 | 10.05 | 11.47 |
| | NASADEM | 13 | 0.92 | -8.59 | 27.47 | 3.48 | 10.71 | 10.86 | 2.08 | 6.05 | 8.97 | 19.27 |
| | SRTMGL1 | 13 | 0.92 | -8.56 | 20.47 | 2.10 | 9.41 | 9.28 | 1.30 | 6.81 | 10.09 | 19.27 |
| | SRTMX | 13 | 0.94 | -16.56 | 41.40 | 1.10 | 15.48 | 14.91 | -1.61 | 8.79 | 13.03 | 13.47 |
| | TDX90 | 13 | 0.91 | -38.87 | 95.80 | 2.97 | 36.24 | 34.95 | -3.88 | 23.68 | 35.11 | 27.29 |
| | TDX4 | 11 | 0.97 | -3.91 | 21.30 | 5.16 | 7.50 | 8.82 | 5.10 | 4.02 | 5.96 | 15.12 |
| 3G | AW3D30 | 70 | 0.97 | -24.34 | 29.00 | -3.04 | 9.92 | 10.30 | -5.18 | 5.98 | 8.87 | 8.48 |
| | GDEM3 | 70 | 0.97 | -28.34 | 21.00 | -4.79 | 10.00 | 11.03 | -4.60 | 5.24 | 7.76 | 10.80 |
| | NASADEM | 70 | 0.97 | -27.34 | 24.00 | -5.67 | 9.57 | 11.06 | -6.27 | 5.31 | 7.87 | 7.77 |
| | SRTMGL1 | 70 | 0.97 | -28.34 | 25.00 | -5.25 | 9.55 | 10.84 | -6.04 | 5.33 | 7.91 | 7.77 |
| | TDX90 | 70 | 0.86 | -44.56 | 51.24 | -4.06 | 24.90 | 25.05 | -4.76 | 17.58 | 26.07 | 32.84 |
| | TDX4 | 70 | 0.99 | -14.84 | 11.91 | -3.80 | 4.72 | 6.03 | -3.66 | 2.82 | 4.18 | 0.40 |
| QD | AW3D30 | 2227 | 0.92 | -12.93 | 11.08 | -3.60 | 4.53 | 5.78 | -2.58 | 2.18 | 3.23 | 2.13 |
| | GDEM3 | 2227 | 0.88 | -21.41 | 36.36 | 5.16 | 14.66 | 15.54 | -0.61 | 9.46 | 14.03 | 25.44 |
| | NASADEM | 2227 | 0.89 | -16.93 | 9.00 | -0.41 | 4.79 | 4.80 | -0.14 | 2.75 | 4.08 | 4.63 |
| | SRTMGL1 | 2227 | 0.89 | -18.93 | 13.29 | -1.60 | 5.69 | 5.91 | -1.06 | 3.50 | 5.18 | 4.49 |
| | TDX90 | 2227 | 0.88 | -23.90 | 12.63 | -1.35 | 7.17 | 7.30 | 0.22 | 2.88 | 4.27 | 5.64 |
| | TDX4 | 2227 | 0.96 | -10.32 | 5.68 | -1.14 | 1.23 | 1.68 | -1.29 | 0.72 | 1.06 | 0.44 |

TDX90. However, the TDX90 has a poor performance in terms of other accuracy measures.

### *C. Coastal Area: Qingdao*

Qingdao is the largest coastal city in Shandong Province, China, and has a continental coastline of more than 700 km with numerous capes and coves along the tortuous coastline. The land cover in this region mainly consists of impervious surface, temperate deciduous, and coniferous broad-leaved forest as well as plenty of cropland as shown in Figs. 3 and 4(e) and (f). Mount Lao (also known as Laoshan Mountain) is the highest coastal mountain in China. It is composed of granite and is located on the southeast coast of Qingdao, near the East Sea. The highest peak is about 1133 m. Faults are mainly developed in NE–NNE as the controlling factor over the structural and geomorphological patterns. The combined impact of rising sea level, storm surges, and land subsidence on coastal areas is increasing, such as severe erosion, frequent inundation, and shorelines retreat, leaving critical infrastructure vulnerable [55]–[57].

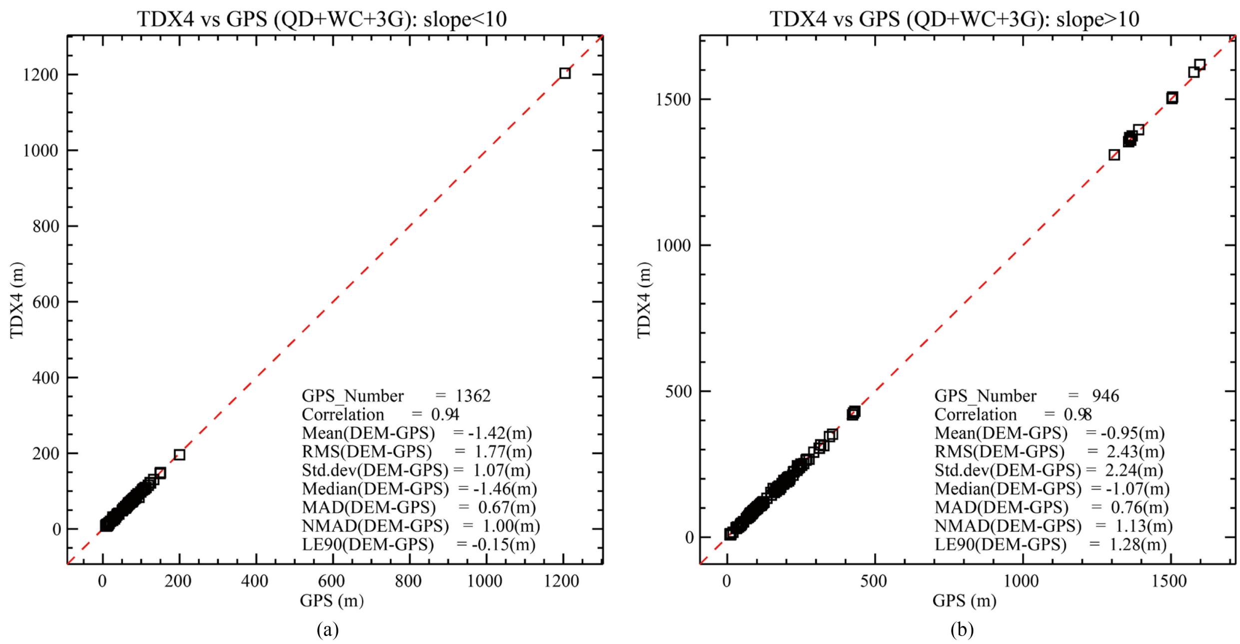


Fig. 7. Scatterplots of TDX4 vs. GPS separated into two slope categories: (a) less than 10° and (b) more than 10° using all the GPS points over all of the three study areas. Red dashed line indicates the perfect fit.

Most of the GPS RTK points are distributed over open areas, e.g., road side and coastal beach [Fig. 4(e)]. TanDEM-X DEM has an rms of 1.7 m and LE90 of 0.4 m, which performs much better than that of the rest of the global DEMs as a whole (Table III). Its NMAD value is almost same with that of STD (1.2 m). However, there is a negative systematic mean bias of 1.1 m, which is slightly larger than that of median differences (−1.3 m).

As shown in Fig. 5(g), the skewness of 0.5 means that the distribution is moderately skewed. A leptokurtic kurtosis of 2.37 represents that the distribution is more peaked than the normal distribution. When compared the datasets of elevation differences to a theoretical normal model, the distribution with a fat tail has both the ends of the Q-Q plot to deviate from the straight line and its center follows a straight line. Outliers are evident at both ends of the range. Similarly, outliers also exist with other global DEMs except for GDEM3, although this data does not perform well in terms of accuracy measures [Fig. 5(i)].

As a whole, the outliers from the above apparently have a strong influence on the estimated ME, STD, and rms. However, the accuracy results of both TanDEM-X DEM and TDX90 in Qingdao coastal areas are superior to those of the other two mountainous areas. Quantiles that are not sensitive to outliers or non-normality of the elevation error distribution are presented in Fig. 5 and Table III. Fig. 6(a) provides the absolute vertical accuracy of TanDEM-X DEM with all 2308 GCPs in total from three study areas. With very few exceptions, most of the errors are concentrated in the range of ±5 m at a height of no more than 500 m [Fig. 6(b)]. If elevation differences are separated into different slopes, one can see the error decreases in areas with low slopes of no more than 10° [Fig. 7(a) and (b)]. The most significant change is that the LE90 is close to zero, whereas the systematic mean offsets from GPS is getting bigger a little bit.

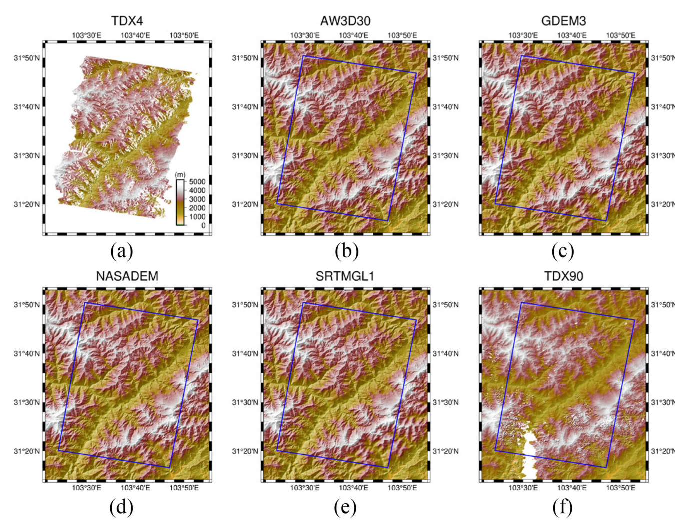


Fig. 8. Shaded relief map over the Wenchuan areas. Blue rectangles represent TanDEM-X SAR data coverage. Note that all the global DEMs have the same pixel grid as TanDEM-X DEM.

## IV. Raster-Based Validation

### A. Visual Inspect

Shaded relief maps are plotted in Figs. 8 –10 for visual inspection. Note that, only a small part of the SRTMX DEM is available in the Wenchuan area due to its crisscrossing image strips, whereas no data in the other two study areas unfortunately.

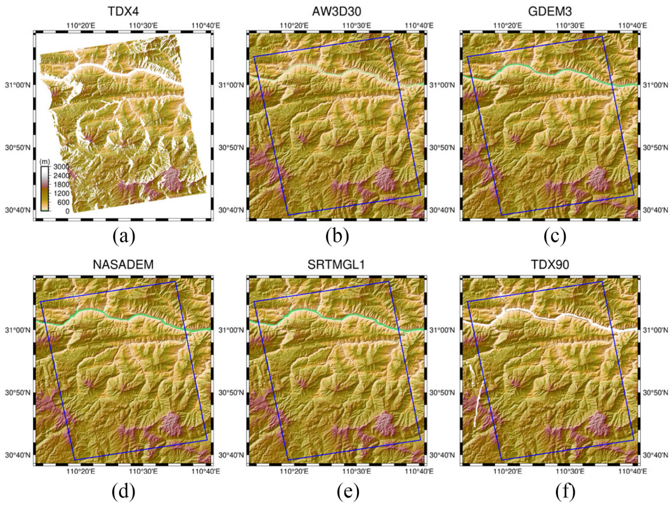


Fig. 9. Shaded relief map over the Three Gorges areas. Blue rectangles represent TanDEM-X SAR data coverage.

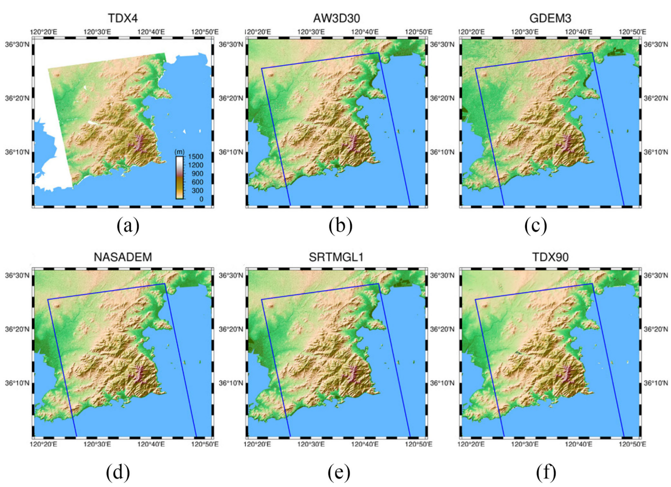


Fig. 10. Shaded relief map over the Qingdao areas. Blue rectangles represent TanDEM-X SAR data coverage.

Therefore, the SRTMX DEM is not included in the following sections.

First, in the mountainous areas with steep slopes (Figs. 8 and 9), InSAR-derived DEMs with single track SAR data are prone to the incoherent effects from shadow and layover as well as dense vegetation cover. Therefore, original TanDEM-X DEM (TDX4 and TDX90) without further edit usually contain plenty of holes and voids affected by phase unwrapping mask. Note that 30 m global DEMs available at present have been filled with other existing DEMs to eliminating the voids, which would be beneficial for those applications where continuous terrain representations are required. Second, GDEM3 and SRTM DEMs that have offered water mask for lakes, rivers, and sea areas can be able to accurately represent continuous geomorphology.

Furthermore, all global DEMs have been resampled and interpolated into the resolution of TDX4 in order to compare with each other. Therefore, some details of the terrains are becoming blurred, such as the Wenchuan mountainous area in the lower right corner for GDEM3 and SRTMGL1 [Fig. 8(c) and (e)]. Due to the low resolution for TDX90 derived from the degradation of 12 m TanDEM-X data, most geomorphological details smoothed become indistinguishable [Figs. 8(f) and (f)]. However, fine complete topographical details are fundamental and critical for sophisticated application scenarios, e.g., high-resolution InSAR image coregistration for the removal of topography phase, terrain matching navigation, and coastal inundation vulnerability evaluation due to sea level rise.

For Qingdao coastal areas (Fig. 10), the topographically related differences are not significant. However, updated high-resolution coastline and building information would certainly facilitate and contribute to more accurate application results, e.g., dynamic storm surge flood modeling.

## *B. Elevation Comparison*

We also performed comparisons of TanDEM-X DEM with other global DEMs listed above in the study areas. As a result of its short X-band radar wavelength, the TanDEM-X DEM should be defined as DSM that includes elevated objects such as vegetation, canopy, and buildings. DEM model-to-model statistical comparisons are shown in Fig. 11 and Table IV, while spatial distributions of elevation differences are presented in Fig. 12.

First, it is pretty obvious that the overall difference between the TanDEM-X DEM and other global DEMs in Qingdao coastal area is much smaller and more concentrated than those in the other two regions (Fig. 11). The values of rms and LE90 are all below 10 m except for those of TDX4 vs TDX90. The TDX4 is most consistent with AW3D30, which has the minimum mean, median, and NMAD difference (0.1, 0.4, and 3.4 m), whereas NASADEM has the best LE90 of 5.3 m.

Second, there are lots of divergent elevation differences in the Three Gorges mountainous area. The elevation of TDX4 is closest to that of SRTMGL1 with almost negligible mean and median difference within $\pm 0.1$ m and the lowest rms and LE90 values of around 10 m.

Third, elevation differences between TDX4 and global DEMs in the Wenchuan mountainous areas are greater than those in the other two areas in terms of, e.g., rms and LE90 values of more than 30 m, although there are relatively low mean and median errors within 10 m. The greatest elevation difference exists between TDX4 and TDX90 in Fig. 11(e1).

Fourth, Fig. 12(a)–(d) shows that most positive elevation differences are systematically concentrated on the right part of the TDX4 descending track in the Wenchuan area, whereas negative ones mostly on the left side. However, it shows a random distribution for TDX4 vs TDX90 [Fig. 12(e)]. It is probably attributed to the result of combined influence from TanDEM-X observation direction, relatively short wavelength, land cover, and fault strike. Comparatively low systematic biases can be found in the upper part in the Three Gorges area and Laoshan Mountain area that is on account of vegetation cover to a large extent.

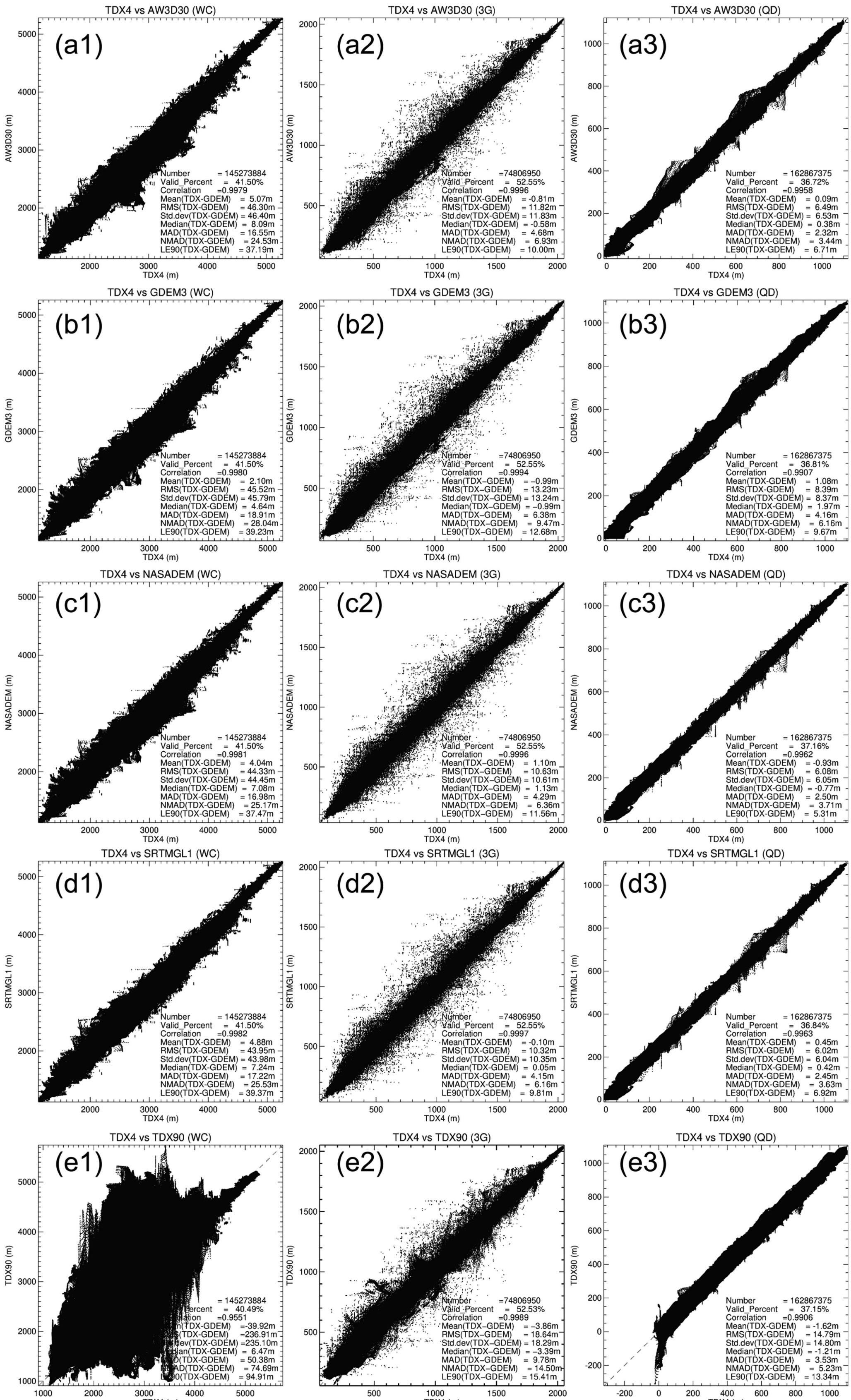


Fig. 11. Scatterplots of TDX4 vs. global DEMs. Five rows represent (a) AW3D30, (b) GDEM3, (c) NASADEM, (d) SRTMGL1, (e) TDX90, while three columns show the three study areas (WC, 3G, and QD). Red dashed line indicates the perfect fit.

TABLE IV
RELATIVE VERTICAL DEM ACCURACY IN THE STUDY AREAS

| Area | TDX4-DEM | Perc. | Corr. | Min (m) | Max (m) | ME (m) | STD (m) | RMS (m) | Median (m) | MAD (m) | NMAD (m) | LE90 (m) |
|---|---|---|---|---|---|---|---|---|---|---|---|---|
| WC | AW3D30 | 41.50% | 0.99 | -737.89 | 923.43 | 5.07 | 46.40 | 46.30 | 8.09 | 16.55 | 24.53 | 37.19 |
| | GDEM3 | 41.50% | 0.99 | -749.51 | 762.77 | 2.10 | 45.79 | 45.52 | 4.64 | 18.91 | 28.04 | 39.23 |
| | NASADEM | 41.45% | 0.99 | -740.51 | 735.39 | 4.04 | 44.45 | 44.33 | 7.08 | 16.98 | 25.17 | 37.47 |
| | SRTMGL1 | 41.45% | 0.99 | -742.51 | 617.78 | 4.88 | 43.98 | 43.95 | 7.24 | 17.22 | 25.53 | 39.37 |
| | SRTMX | 37.66% | 0.99 | -833.27 | 4454.88 | 0.39 | 121.58 | 120.62 | 7.09 | 22.92 | 33.98 | 43.85 |
| | TDX90 | 40.49% | 0.96 | -2865.84 | 2553.74 | -39.92 | 235.10 | 236.91 | 6.47 | 50.38 | 74.69 | 94.91 |
| 3G | AW3D30 | 52.55% | 0.99 | -718.71 | 642.24 | -0.81 | 11.83 | 11.82 | -0.58 | 4.68 | 6.93 | 10.00 |
| | GDEM3 | 52.55% | 0.99 | -720.71 | 628.07 | -0.99 | 13.24 | 13.23 | -0.99 | 6.38 | 9.47 | 12.68 |
| | NASADEM | 52.55% | 0.99 | -723.71 | 644.09 | 1.10 | 10.61 | 10.63 | 1.13 | 4.29 | 6.36 | 11.56 |
| | SRTMGL1 | 52.55% | 0.99 | -731.71 | 659.24 | -0.10 | 10.35 | 10.32 | 0.05 | 4.15 | 6.16 | 9.81 |
| | TDX90 | 52.53% | 0.99 | -729.06 | 660.74 | -3.86 | 18.29 | 18.64 | -3.39 | 9.78 | 14.50 | 15.41 |
| QD | AW3D30 | 36.72% | 0.99 | -142.73 | 139.20 | 0.09 | 6.53 | 6.49 | 0.38 | 2.32 | 3.44 | 6.71 |
| | GDEM3 | 36.81% | 0.99 | -126.34 | 103.36 | 1.08 | 8.37 | 8.39 | 1.97 | 4.16 | 6.16 | 9.67 |
| | NASADEM | 37.16% | 0.99 | -78.86 | 135.20 | -0.93 | 6.05 | 6.08 | -0.77 | 2.50 | 3.71 | 5.31 |
| | SRTMGL1 | 36.84% | 0.99 | -96.82 | 144.75 | 0.45 | 6.04 | 6.02 | 0.42 | 2.45 | 3.63 | 6.92 |
| | TDX90 | 60497313 | 0.99 | -167.32 | 289.74 | -1.62 | 14.80 | 14.79 | -1.21 | 3.53 | 5.23 | 13.34 |

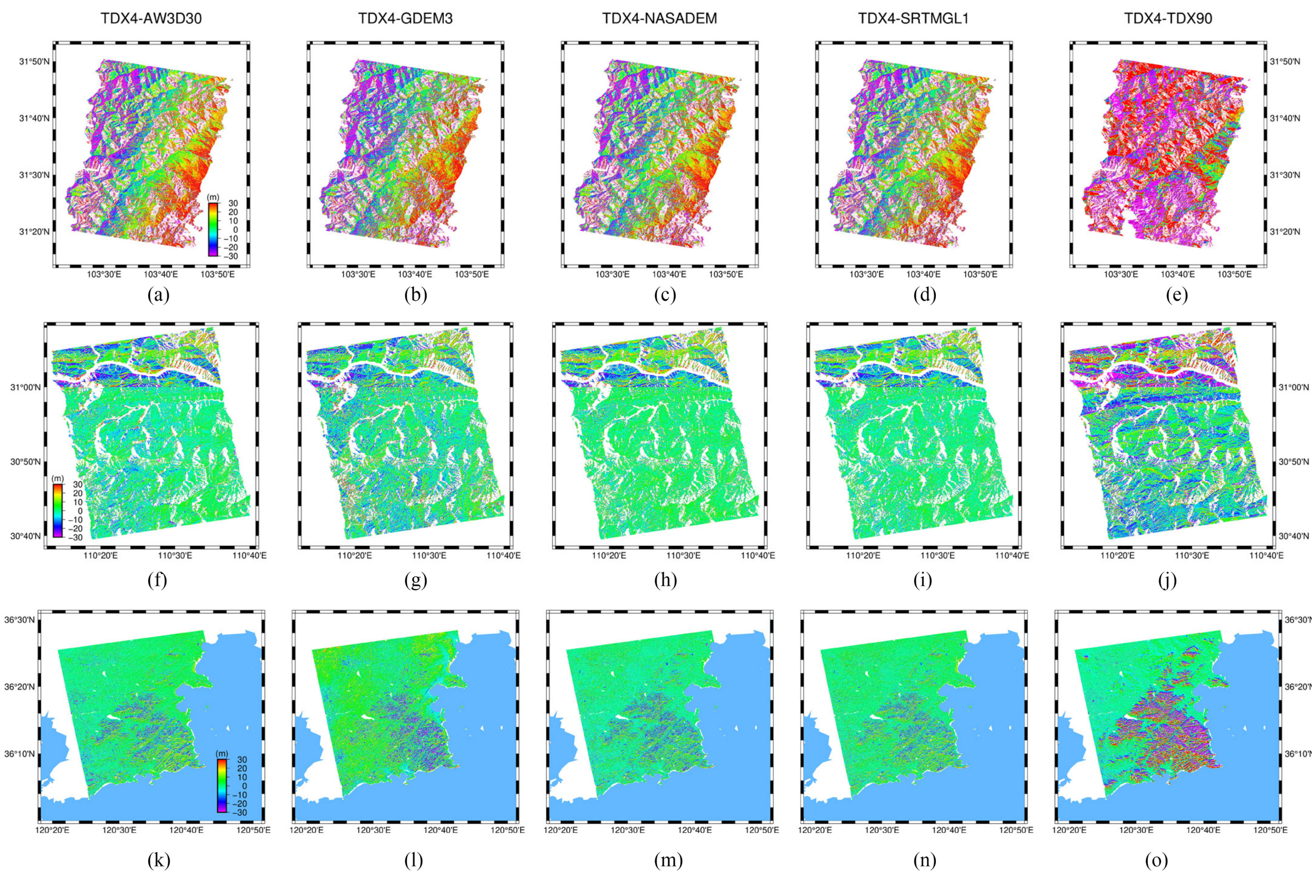


Fig. 12. Shaded DEM difference map of the three study areas.

## C. Slope Comparison

By contrast, slope differences and spatial distribution are presented in Fig. 13 and Table V. Significant systemic bias can also be found in the Wenchuan mountainous area and the Mount Lanshan. Table V shows that slope differences between TDX4 and 30 m global DEMs perform best in the Qingdao coastal area in terms of median values within 1° and LE90 differences around 15°, while rms and LE90 values may reach 15–20 and 20–40°, respectively, in the other two mountainous areas.

## D. Landcover Analysis

In order to evaluate relationship between elevation error and land cover, the height differences (TDX4-GPS) are hence separated into different land cover classes to investigate the spatial

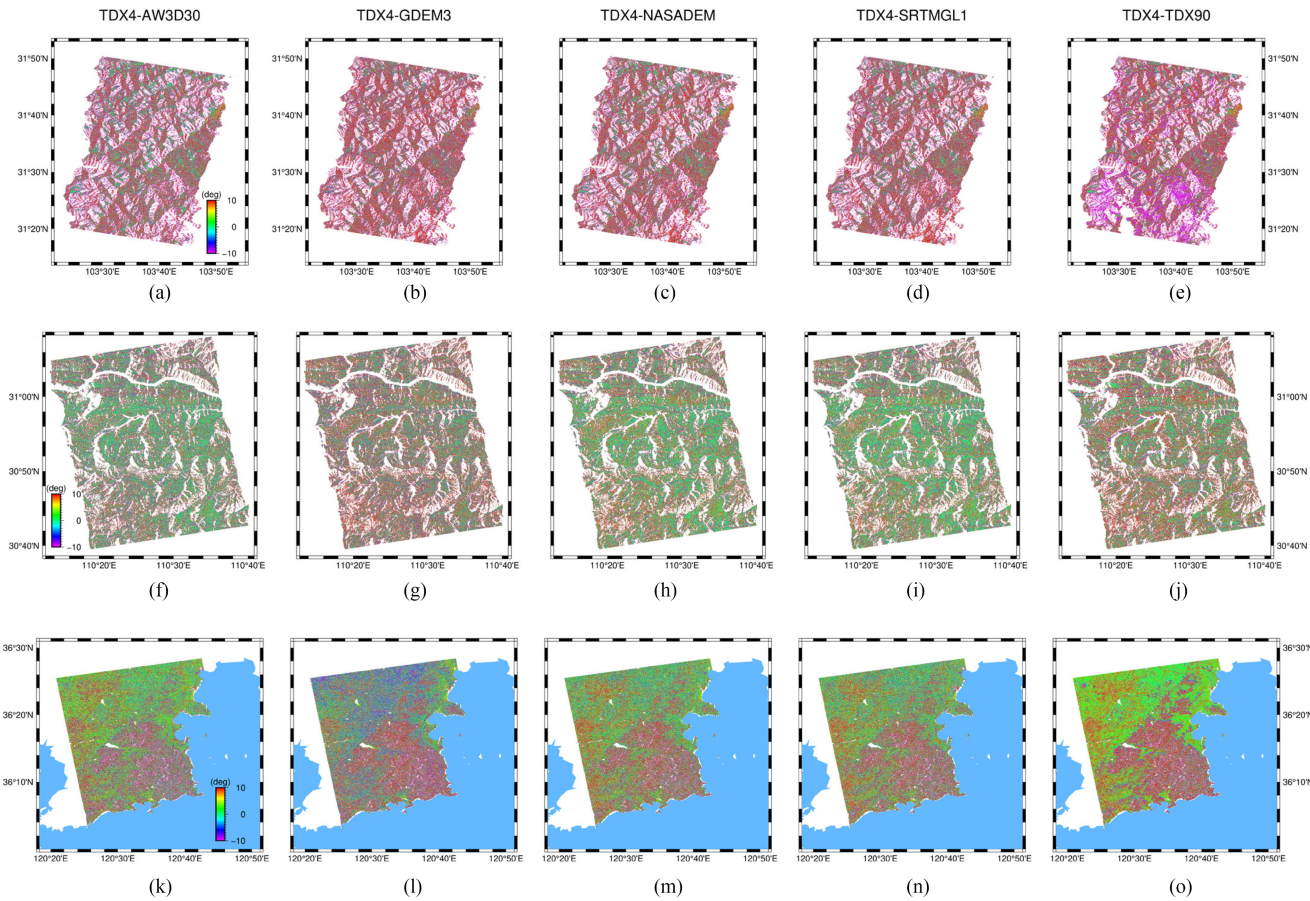


Fig. 13. Shaded slope difference map of the three study areas.

TABLE V
DEM Slope Comparisons in the Study Areas

| Area | TDX4-DEM | Perc. | Corr. | Mean (deg) | Mean (deg) | ME (deg) | STD (deg) | RMS (deg) | Median (deg) | MAD (deg) | NMAD (deg) | LE90 (deg) |
|---|---|---|---|---|---|---|---|---|---|---|---|---|
| WC | AW3D30 | 56315517 | 0.47 | 40.56 | 39.57 | 0.99 | 15.23 | 15.18 | 1.30 | 8.78 | 13.02 | 19.43 |
| | GDEM3 | 56322693 | 0.37 | 40.55 | 36.96 | 3.59 | 16.93 | 17.23 | 3.32 | 10.44 | 15.48 | 24.91 |
| | NASADEM | 56310474 | 0.40 | 40.56 | 37.58 | 2.99 | 16.35 | 16.54 | 2.88 | 9.64 | 14.30 | 23.19 |
| | SRTMGL1 | 56304181 | 0.39 | 40.56 | 37.41 | 3.16 | 16.59 | 16.81 | 2.90 | 9.88 | 14.65 | 23.89 |
| | SRTMX | 51362303 | 0.35 | 40.20 | 40.08 | 0.15 | 18.09 | 18.01 | 0.64 | 10.26 | 15.22 | 22.05 |
| | TDX90 | 55087426 | 0.30 | 40.38 | 41.25 | -0.97 | 20.38 | 20.31 | 0.39 | 12.06 | 17.89 | 23.39 |
| 3G | AW3D30 | 41256097 | 0.64 | 35.35 | 27.93 | 7.34 | 18.85 | 20.11 | 2.55 | 6.26 | 9.29 | 36.36 |
| | GDEM3 | 41206189 | 0.53 | 35.35 | 26.37 | 8.90 | 20.09 | 21.86 | 3.97 | 7.88 | 11.68 | 38.97 |
| | NASADEM | 41225497 | 0.63 | 35.36 | 26.63 | 8.65 | 19.09 | 20.84 | 3.46 | 6.15 | 9.12 | 37.48 |
| | SRTMGL1 | 41235802 | 0.64 | 35.36 | 26.83 | 8.45 | 18.99 | 20.66 | 3.25 | 5.98 | 8.87 | 36.90 |
| | TDX90 | 41367966 | 0.54 | 35.27 | 25.75 | 9.41 | 19.88 | 21.88 | 9.41 | 7.38 | 10.95 | 40.52 |
| QD | AW3D30 | 41708201 | 0.72 | 19.57 | 17.91 | 1.59 | 9.87 | 9.96 | 0.51 | 5.12 | 7.60 | 13.68 |
| | GDEM3 | 49556715 | 0.61 | 17.47 | 16.48 | 0.92 | 10.82 | 10.81 | -0.73 | 5.66 | 8.39 | 14.97 |
| | NASADEM | 42394002 | 0.70 | 19.06 | 16.24 | 2.75 | 9.90 | 10.23 | 1.12 | 5.36 | 7.95 | 15.50 |
| | SRTMGL1 | 42392107 | 0.70 | 19.06 | 16.52 | 2.47 | 9.99 | 10.25 | 0.92 | 5.38 | 7.98 | 15.25 |
| | TDX90 | 59832983 | 0.66 | 15.88 | 10.23 | 5.60 | 10.00 | 11.39 | 4.04 | 4.33 | 6.42 | 18.16 |

patterns of error and assess the impacts of vegetation on DEM quality. The latest 10 m resolution global land cover map named FROM-GLC10 v0.1.3 that has been developed from Sentinel-2 images acquired in 2017 with the random forest classifier are adopted in this article [58]. There are 10 classes, that is, cropland, forest, grassland, shrubland, wetland, water body, tundra, impervious area, bare land, snow and ice, in the first level classification scheme of FROM-GLC10. For the TDX4-GPS, only five land cover classes are relevant shown in Fig. 14 and Table VI.

Negative systematic mean biases exist in four land cover classes except for the bareland, whereas there are negative median elevation differences in the cropland, grassland, impervious surface, and bareland, except for the forest close to zero. However, it is obvious that elevation accuracy gradually

TABLE VI
ABSOLUTE DEM VERTICAL ACCURACY SEPARATED INTO FIVE LAND COVER CLASSES IN THE STUDY AREAS

| Area | Landcover | GPS No. | Corr. | Min (m) | Max (m) | ME (m) | STD (m) | RMS (m) | Median (m) | MAD (m) | NMAD (m) | LE90 (m) |
|---|---|---|---|---|---|---|---|---|---|---|---|---|
| Total | Cropland | 45 | 0.99 | -15.30 | 8.15 | -2.90 | 4.30 | 5.14 | -2.63 | 1.88 | 2.79 | 1.87 |
| | Forest | 173 | 0.99 | -12.15 | 12.60 | -0.23 | 2.48 | 2.49 | 0.01 | 0.96 | 1.43 | 1.65 |
| | Grassland | 780 | 0.85 | -8.66 | 17.12 | -1.47 | 1.67 | 2.22 | -1.67 | 0.78 | 1.16 | 1.13 |
| | Impervious surface | 1300 | 0.87 | -4.93 | 5.37 | -1.29 | 0.99 | 1.63 | -1.29 | 0.60 | 0.89 | -0.18 |
| | Bareland | 10 | 0.99 | -10.62 | 26.08 | 0.16 | 9.75 | 9.25 | -1.75 | 3.01 | 4.47 | 1.88 |

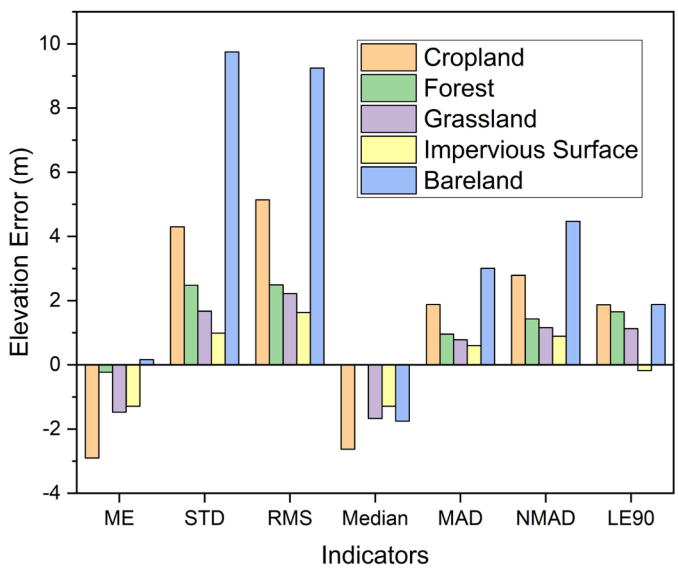


Fig. 14. Land-cover class assessment for the elevation differences of TDX4-GPS over the three study areas in total.

decreases in the three vegetation classes from grassland, forest to cropland in terms of STD, rms, NMAD, and LE90 values. As a whole, accuracy performs best in impervious surface with rms of 1.6 m and LE90 near zero. Note that, relatively large anomalies in the bareland could be affected by the small number of sampling points.

## V. DISCUSSION

### A. Systematic Errors

In this article, the overall absolute vertical accuracy of the high-resolution TanDEM-X DEM evaluated with accurate GPS measurements is 1.7 m, which is largely consistent with the DLR official validation report [22], [23] as well as most of the independent results in other areas outside of China [2], [6], [8], [19], [24], [25], [29], [59]. As a DSM, the TanDEM-X DEM does not represent the bare earth surface in those areas with vegetation and man-made objects, e.g., cropland and buildings. Although negative bias with an overall ME in the vegetated areas remains uncertainty, LE90 accuracy measures that are not sensitive to the large outliers reveal a relatively objective result of a 1–2 m positive offset except for the steep slopes (Figs. 7 and 14).

The comparisons between the TanDEM-X DEM and other global DEMs over mountainous areas represent strong systematic bias, which are greatly influenced by phase unwrapping errors and different signal penetration depth over vegetation canopy [23]. In those regions, more data voids can be seen in the InSAR-derived TanDEM-X DEM than the 30 m global DEMs currently available, e.g., AW3D30 and GDEM3. Areas with low coherences due to e.g., steep slope and dense vegetation have been masked as voids or invalid data. No void filling or interpolation for missing height values has been applied to the current TanDEM-X DEM. There are large numbers of voids in those incoherent regions where coherence is lower than the threshold for the mountainous areas [Figs. 8(a), 9(a), and 10(a)]. However, the vegetation coverage in Qingdao Laoshan mountainous area is much lower than that in Wenchuan and Three Gorges areas due to low precipitation and exposed rocks, which makes the effect of shadow more significant than that of vegetation.

The bistatic stripmap mode that can be able to provide simultaneous data acquisition avoids possible errors from temporal decorrelation and atmospheric disturbances [21]. If the overall direction and slope of the mountain are perpendicular to the direction of the radar satellite's flight orbit, it will be beneficial to receive more ground scattering echoes. Therefore, it is still possible to maintain a high coherence at the top of the mountain so as to obtain reliable height observation. It would be a viable approach to derive the nonvoid continuous TanDEM-X DEM from the elevation integration of existing high-precision high resolution DEMs or data from other viewing geometries in those void areas with shadow and layover. On the contrary, global DEMs obtained by optical sensors, e.g., ASTER or ALOS PRISM, cannot provide reliable elevation values in areas with extensive cloud coverage, while InSAR-derived DEMs may be the only source capable of providing the necessary observations for void filling. However, there is a large elevation difference between the two types of data in mountainous areas or areas with persistent cloud cover.

Water surfaces that are not delineated or flattened are also masked as voids for TanDEM-X DEM and TDX90. However, the near-global water body dataset (ASTWBD) is an advantage to delineate minimum water bodies of 0.2 km$^2$ for the improved GDEM3 [38]. Besides, SRTMGL1 and NASADEM have used the GDEM2 and GDEM3 water mask, respectively, as a guide to repair the SRTM water body dataset (SWBD), especially for overlapping areas of steep coastal mountains and flat offshore water. In addition, AW3D30 can provide a binary water or no water mask for land water as well as using the SWBD for sea mask.

The results of TDX90 DEM are mainly influenced by the current nonedit release. As a product variant of the TanDEM-X 12m DEM (Version 1.0), the processing artifacts and outliers

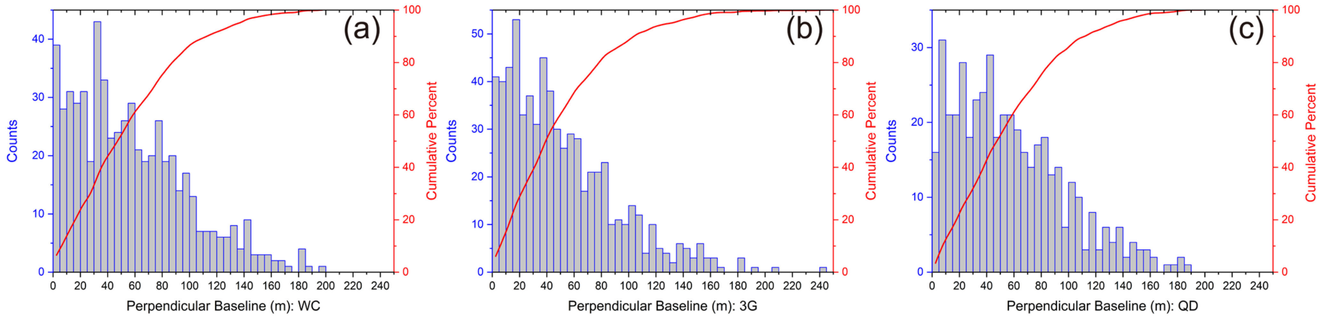


Fig. 15. Histogram and cumulative percent of perpendicular baselines from Sentienl-1 InSAR pairs over the three study areas (WC, 3G, and QD).

TABLE VII
SENTINEL-1 SAR DATA DETAILS USED IN THE STUDY AREAS

| Area | Flight Direction | Beam Mode | Path | Frame | Time Span | Perpendicular Baseline Limit | Temporal Baseline Limit | Scenes | Pairs |
|---|---|---|---|---|---|---|---|---|---|
| WC | Ascending | IW | 128 | 99 | 2014/10/14-2020/08/07 | 300 m | 60 days | 143 | 602 |
| 3G | Ascending | IW | 84 | 95 | 2015/04/09-2020/08/16 | 300 m | 60 days | 145 | 676 |
| QD | Descending | IW | 76 | 473 | 2015/07/01-2020/08/09 | 300 m | 60 days | 108 | 461 |

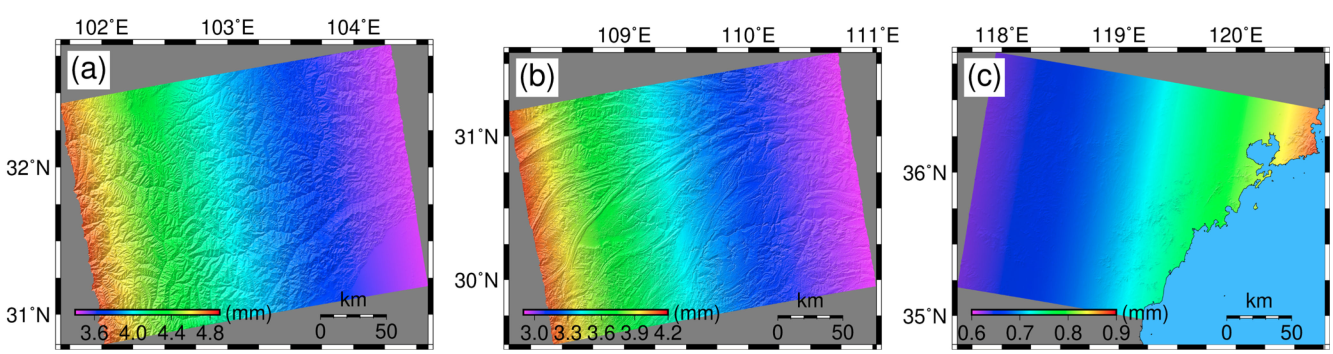


Fig. 16. 2-D simulation of InSAR deformation uncertainty over the three study areas (WC, 3G, and QD).

definitely lead to unreliable TDX90 height values in those noisy mountainous areas, e.g., water surfaces, steep slopes, and dense vegetation [2], [25].

## *B. Contribution to InSAR Deformation Monitoring*

Differential InSAR images are widely used to detect deformation associated with various geophysical phenomena, e.g., land subsidence, movements from landslides, fault, volcano, and glacier, as well as other surface deformation processes [11], [60], [61]. However, it is challenging to use InSAR technique to observe subtle nonlinear deformation signal extending large areas due to error sources, e.g., temporal and geometry decorrelation, topographic, and atmospheric contributions [62]. Advanced InSAR time series analysis methods, e.g., persistent scatterer and small baseline subsets (SBAS), have been developed to overcome the major error effects [63]–[65]. Here, we use the Sentinel-1 interferometric wide-swath (IWS) datasets to investigate the topography effects on the SBAS analysis in the three study areas.

In InSAR deformation monitoring, the phase caused by external DEM error still remains in the differential interferograms after the topographic phase removal. The impact of the topographic error on the estimated displacement is proportional to the perpendicular baseline history of the set of SAR acquisitions [66]. According to the law of error propagation [67], there is a linear relationship between perpendicular baseline and deformation uncertainty introduced by DEM error. A simple simulation of topographic contribution to deformation uncertainty can be described as follows [11], [61], [66], [68]:

$$\sigma_{\Delta\rho} = \frac{B_{\perp}}{R \sin\theta} \sigma_{\mathrm{DEM}} \tag{8}$$

where $B_{\perp}$ is perpendicular baseline, $R$ is satellite orbit height, $\theta$ is incidence angle, $\sigma_{\Delta\rho}$ and $\sigma_{\mathrm{DEM}}$ are the uncertainties of deformation and topography.

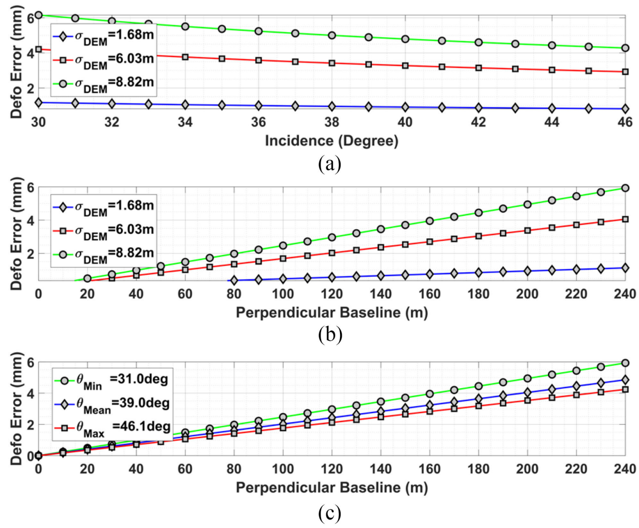


Fig. 17. 1-D simulation of InSAR deformation uncertainty over the three study areas. Note that the perpendicular baseline is based on a baseline maximum of 240 m for the first plot. Orbit height of Sentinel-1 is 693 km.

Fig. 15 shows that the spatial perpendicular baselines within 100 m can reach 80% for all the three Sentinel-1 data tracks (Table VII). In addition to the baseline range, we use the Sentinel-1 incidence and rms value of TanDEM-X DEM in the study areas to make 1-D and 2-D simulation. All the incidence files are generated from Sentinel-1 IWS data with European Space Agency Sentinel Application Platform. With regard to a constant topographic error, both Figs. 16 and 17 indicate that the major influence comes from the perpendicular baseline. Given a constant TanDEM-X DEM error of 8.8 m, it turns out that the 80% interferometric pairs have a low topographic contribution within 2.5 mm for the Wenchuan mountainous area, whereas this would be negligible for the Qingdao coastal area with a DEM error of 1.7 m.

## VI. Conclusion

In this article, the high-resolution TanDEM-X DEMs are generated from the CoSSC scenes with two rounds of iteration method in the mountainous and coastal area of China. We used high-precision GPS measurements and freely available global DEMs (AW3D30 v2.2, ASTER GDEM v3, SRTM v3.1, NASADEM, X-band SRTM, and TDX90 DEM) to evaluate the vertical accuracy of TanDEM-X DEM. The correlation between height differences and slope derivatives was then investigated. Furthermore, the elevation differences were separated into different land cover classes from the 10 m global land cover dataset to investigate the spatial patterns of DEM error. Finally, taking Sentinel-1 SBAS as an example, topography contribution was simulated to detect InSAR deformation uncertainty.

We find that the robust metrics, e.g., NMAD and LE90, are more resistant to the presence of outliers. The results demonstrate remarkable elevation quality and consistency in the coastal areas with RMSE of 1.7 m and LE90 of 0.4 m, whereas 3–4 times weaker accuracies in steep slope mountainous areas. The results show that a 1–2 m positive offset for LE90 accuracy measures that are not sensitive to the large outliers except for steep slopes. It indicates that TanDEM-X DEM is generally superior to other global DEMs and presents an excellent consistence with SRTM C-band DEM in coastal areas. Simulation reveals a low or even negligible topographic error contribution from TanDEM-X DEM with 2–4 mm in mountainous areas and less than 1 mm in coastal areas.

With its unprecedented resolution generated from bistatic X-band interferometric SAR acquisitions, the TanDEM-X DEMs are expected to be an excellent source of topography for various global scientific and engineering applications, e.g., land subsidence, movements from landslides, fault, volcano, and glacier, coastal vulnerability, and geomorphological mapping. It would be greatly beneficial to the societal benefit areas (disaster, health, energy, climate, weather, ecosystem, agriculture, and biodiversity) defined by the Global Earth Observation System of System.

## Acknowledgment

The authors would like to thank Dr. Yingbing Li and those colleagues from Wuhan University, Southwest Jiaotong University and Ocean University of China for conducting GNSS field measurements in the three study areas. All the TanDEM-X SAR data were provided under DLR TanDEM-X AO Project (DEM_CALVAL1423; IDEM_CALVAL0059). Authors were also grateful to NASA, METI, USGS, and DLR for providing the free ASTER GDEM v3, AW3D30, C- and X-band SRTM DEM, and TanDEM-X 90m DEMs, respectively. Meanwhile, they sincerely thank the editors and all anonymous reviewers for their constructive and excellent reviews that greatly improve the article quality.

## References

[1] S. J. Boulton and M. Stokes, "Which DEM is best for analyzing fluvial landscape development in mountainous terrains?," *Geomorphology*, vol. 310, pp. 168–187, 2018.

[2] L. Hawker, J. Neal, and P. Bates, "Accuracy assessment of the TanDEM-X 90 digital elevation model for selected floodplain sites," *Remote Sens. Environ.*, vol. 232, 2019, Art. no. 111319.

[3] G. Li, H. Lin, and Q. Ye, "Heterogeneous decadal glacier downwasting at the mt. Everest (Qomolangma) from 2000 to ∼2012 based on multi-baseline bistatic SAR interferometry," *Remote Sens. Environ.*, vol. 206, pp. 336–349, 2018.

[4] J. Neelmeijer, M. Motagh, and B. Bookhagen, "High-resolution digital elevation models from single-pass TanDEM-X interferometry over mountainous regions: A case study of Inylchek glacier, central Asia," *ISPRS J. Photogramm. Remote Sens.*, vol. 130, pp. 108–121, 2017.

[5] I. Pipaud, D. Loibl, and F. Lehmkuhl, "Evaluation of TanDEM-X elevation data for geomorphological mapping and interpretation in high mountain environments—A case study from SE Tibet, China," *Geomorphology*, vol. 246, pp. 232–254, 2015.

[6] M. d. R. González-Moradas and W. Viveen, "Evaluation of ASTER GDEM2, SRTMv3.0, ALOS AW3D30 and TanDEM-X DEMs for the Peruvian Andes against highly accurate GNSS ground control points and geomorphological-hydrological metrics," *Remote Sens. Environ.*, vol. 237, 2020, Art. no. 111509.

[7] D. C. Mason, M. Trigg, J. Garcia-Pintado H. L. Cloke, J. C. Neal, and P. D. Bates, "Improving the TanDEM-X digital elevation model for flood modelling using flood extents from synthetic aperture radar images," *Remote Sens. Environ.*, vol. 173, pp. 15–28, 2016.

[8] R. Avtar, A. P. Yunus, S. Kraines, and M. Yamamuro, "Evaluation of DEM generation based on interferometric SAR using TanDEM-X data in Tokyo," *Phys. Chem. Earth, Parts A/B/C*, vol. 83–84, pp. 166–177, 2015.

[9] M. H. Braun *et al.*, "Constraining glacier elevation and mass changes in South America," *Nat. Climate Change*, vol. 9, no. 2, pp. 130–136, 2019.

[10] J. Brock, P. Schratz, H. Petschko J. Msuenchow, M. Micu, and A. Brenning, "The performance of landslide susceptibility models critically depends on the quality of digital elevation models," *Geomatics, Natural Hazards Risk*, vol. 11, no. 1, pp. 1075–1092, 2020.

[11] R. Bürgmann, P. A. Rosen, and E. J. Fielding, "Synthetic aperture radar interferometry to measure earth's surface topography and its deformation," *Annu. Rev. Earth Planet. Sci.*, vol. 28, no. 1, pp. 169–209, 2000.

[12] D. B. Gesch, "Consideration of vertical uncertainty in elevation-based sea-level rise assessments: Mobile bay, Alabama case study," *J. Coastal Res.*, vol. 10063, no. 63, pp. 197–210, 2013.

[13] "The shuttle radar topography mission (SRTM) collection user guide," NASA, 2015. [Online]. Available: https://lpdaac.usgs.gov/sites/default/files/public/measures/docs/NASA_SRTM_V3.pdf

[14] "DLR SRTM X-SAR digital elevation models," DLR, 2012. [Online]. Available: https://centaurus.caf.dlr.de:8443/eoweb-ng/licenseAgreements/DLR_ SRTM_Readme.pdf

[15] J. A. Slater *et al.*, "Global assessment of the new ASTER global digital elevation model," *Photogramm. Eng. Remote Sens.*, vol. 77, no. 4, pp. 335–349, 2011.

[16] E. Rodriguez, C. S. Morris, and J. E. Belz, "A global assessment of the SRTM performance," *Photogramm. Eng. Remote Sens.*, vol. 72, no. 3, pp. 249–260, 2006.

[17] P. Li, Z. Li, J.-P. Muller, C. Shi, and J. Liu, "A new quality validation of global digital elevation models freely available in China," *Surv. Rev.*, vol. 48, no. 351, pp. 409–420, 2016.

[18] P. Li, C. Shi, Z. Li, J. P. Muller, J. Drummond, and X. Li, "Evaluation of ASTER GDEM using GPS benchmarks and SRTM in China," *Int. J. Remote Sens.*, vol. 34, no. 5, pp. 1744–1771, 2013.

[19] C. H. Grohmann, "Evaluation of TanDEM-X DEMs on selected Brazilian sites: Comparison with SRTM, ASTER GDEM and ALOS AW3D30," *Remote Sens. Environ.*, vol. 212, pp. 121–133, 2018.

[20] J. Takaku, T. Tadono, K. Tsutsui, and M. Ichikawa, "Quality improvements of 'AW3D' global DSM derived from ALOS prism," in *Proc. IEEE Int. Geosci. Remote Sens. Symp.*, 2018, pp. 1612–1615.

[21] M. Zink *et al.*, "TanDEM-X: The new global DEM takes shape," *IEEE Geosci. Remote Sens. Mag.*, vol. 2, no. 2, pp. 8–23, Jun. 2014.

[22] P. Rizzoli *et al.*, "Generation and performance assessment of the global TanDEM-X digital elevation model," *ISPRS J. Photogramm. Remote Sens.*, vol. 132, pp. 119–139, 2017.

[23] B. Wessel, M. Huber, C. Wohlfart, U. Marschalk, D. Kosmann, and A. Roth, "Accuracy assessment of the global TanDEM-X digital elevation model with GPS data," *ISPRS J. Photogramm. Remote Sens.*, vol. 139, pp. 171–182, 2018.

[24] J. Baade and C. Schmullius, "TanDEM-X IDEM precision and accuracy assessment based on a large assembly of differential GNSS measurements in Kruger national park, South Africa," *ISPRS J. Photogramm. Remote Sens.*, vol. 119, pp. 496–508, 2016.

[25] A. O. Altunel, "Evaluation of TanDEM-X 90 m digital elevation model," *Int. J. Remote Sens.*, vol. 40, no. 7, pp. 2841–2854, 2019.

[26] J. Bueso-Bello, M. Martone, P. Prats-Iraola, and B. Bräutigam, "First characterization and performance evaluation of bistatic TanDEM-X experimental products," *IEEE J. Sel. Topics Appl. Earth Observ. Remote Sens.*, vol. 9, no. 3, pp. 1058–1071, Mar. 2016.

[27] K. Becek, W. Koppe, and Ş. Kutoğlu, "Evaluation of vertical accuracy of the worlddem$^{\mathrm{TM}}$ using the runway method," *Remote Sens.*, vol. 8, no. 11, 2016, Art. no. 934.

[28] S. Lee and J. Ryu, "High-accuracy tidal flat digital elevation model construction using TanDEM-X science phase data," *IEEE J. Sel. Topics Appl. Earth Observ. Remote Sens.*, vol. 10, no. 6, pp. 2713–2724, Jun. 2017.

[29] K. Zhang *et al.*, "Accuracy assessment of ASTER, SRTM, ALOS, and TDX DEMs for Hispaniola and implications for mapping vulnerability to coastal flooding," *Remote Sens. Environ.*, vol. 225, pp. 290–306, 2019.

[30] C. Rossi, F. R. Gonzalez, T. Fritz, N. Yague-Martinez, and M. Eineder, "TanDEM-X calibrated raw DEM generation," *ISPRS J. Photogramm. Remote Sens.*, vol. 73, pp. 12–20, 2012.

[31] K. Dai *et al.*, "Monitoring activity at the daguangbao mega-landslide (China) using Sentinel-1 TOPS time series interferometry," *Remote Sens. Environ.*, vol. 186, pp. 501–513, 2016.

[32] S. Duque *et al.*, "TanDEM-X payload ground segment: CoSSC generation and interferometric considerations," Tech. Rep. TD-PGS-TN-3129, DLR-German Aerospace Center, Cologne, Germany, 2012.

[33] F. Lemoine *et al.*, "The development of the joint NASA GSFC and national imagery and mapping agency (NIMA) geopotential model EGM96," Tech. Rep. NASA/TP-1998-206861, NASA Goddard Space Flight Center, Greenbelt, MD, USA, 1998.

[34] P. Li *et al.*, "Impacts of geoid height on large-scale crustal deformation mapping with InSAR observations," *Chin. J. Geophys.*, vol. 56, no. 6, pp. 1857–1867, 2013.

[35] R. M. Goldstein and C. L. Werner, "Radar interferogram filtering for geophysical applications," *Geophys. Res. Lett.*, vol. 25, no. 21, pp. 4035–4038, 1998.

[36] A. M. Guarnieri, P. Guccione, P. Pasquali, and Y. L. Desnos, "Multimode ENVISAT ASAR interferometry: Techniques and preliminary results," *IEE Proc. Radar, Sonar Navigation*, vol. 150, no. 3, pp. 193–200, Jun. 2003.

[37] A. Pepe and R. Lanari, "On the extension of the minimum cost flow algorithm for phase unwrapping of multitemporal differential SAR interferograms," *IEEE Trans. Geosci. Remote Sens.*, vol. 44, no. 9, pp. 2374–2383, Sep. 2006.

[38] M. Abrams, R. Crippen, and H. Fujisada, "ASTER global digital elevation model (GDEM) and ASTER global water body dataset (ASTWBD)," *Remote Sens.*, vol. 12, no. 7, 2020, Art. no. 1156.

[39] S. M. Buckley, P. S. Agram, J. E. Belz, and R. E. Crippen, "NASADEM merged DEM global 1 arc second V001," 2020. [Online]. Available: https://lpdaac.usgs.gov/documents/592/NASADEM_User_Guide_V1.pdf

[40] T. G. Farr *et al.*, "The shuttle radar topography mission," *Rev. Geophys.*, vol. 45, no. 2, 2007, Art. no. RG2004.

[41] P. F. Fisher and N. J. Tate, "Causes and consequences of error in digital elevation models," *Prog. Phys. Geogr.*, vol. 30, no. 4, pp. 467–489, 2006.

[42] J. Höhle and M. Höhle, "Accuracy assessment of digital elevation models by means of robust statistical methods," *ISPRS J. Photogramm. Remote Sens.*, vol. 64, no. 4, pp. 398–406, 2009.

[43] K. Dai *et al.*, "Entering the era of earth observation-based landslide warning systems: A novel and exciting framework," *IEEE Geosci. Remote Sens. Mag.*, vol. 8, no. 1, pp. 136–153, Mar. 2020.

[44] Y. Yin, F. Wang, and P. Sun, "Landslide hazards triggered by the 2008 Wenchuan earthquake, Sichuan, China," *Landslides*, vol. 6, no. 2, pp. 139–152, 2009.

[45] R. N. Parker *et al.*, "Mass wasting triggered by the 2008 Wenchuan earthquake is greater than orogenic growth," *Nat. Geosci.*, vol. 4, no. 7, pp. 449–452, 2011.

[46] Z. K. Shen *et al.*, "Slip maxima at fault junctions and rupturing of barriers during the 2008 Wenchuan earthquake," *Nat. Geosci.*, vol. 2, no. 10, pp. 718–724, 2009.

[47] Q. Wang *et al.*, "Rupture of deep faults in the 2008 Wenchuan earthquake and uplift of the Longmen Shan," *Nat. Geosci.*, vol. 4, no. 9, pp. 634–640, 2011.

[48] X. Xu *et al.*, "Coseismic reverse- and oblique-slip surface faulting generated by the 2008 mw 7.9 Wenchuan earthquake, China," *Geology*, vol. 37, no. 6, pp. 515–518, 2009.

[49] L. M. Highland, "Geographical overview of the three Gorges dam and reservoir, China—Geologic Hazards and environmental impacts," Open-File Report 2008-1241, U.S. Department of the Interior, U.S. Geological Survey, 2008.

[50] R. Tomás, Z. Li, P. Liu, A. Singleton, T. Hoey, and X. Cheng, "Spatiotemporal characteristics of the huangtupo landslide in the three Gorges region (China) constrained by radar interferometry," *Geophys. J. Int.*, vol. 197, no. 1, pp. 213–232, 2014.

[51] H. Miao, G. Wang, K. Yin, T. Kamaib, and Y. Li, "Mechanism of the slow-moving landslides in Jurassic red-strata in the three Gorges reservoir, China," *Eng. Geol.*, vol. 171, pp. 59–69, 2014.

[52] A. Singleton, Z. Li, T. Hoey, and J.-P. Muller, "Evaluating sub-pixel offset techniques as an alternative to D-InSAR for monitoring episodic landslide movements in vegetated terrain," *Remote Sens. Environ.*, vol. 147, pp. 133–144, 2014.

[53] P. Liu *et al.*, "Using advanced InSAR time series techniques to monitor landslide movements in badong of the three Gorges region, China," *Int. J. Appl. Earth Observ. Geoinf.*, vol. 21, pp. 253–264, 2013.

[54] X. Shi, H. Jiang, L. Zhang, and M. Liao, "Landslide displacement monitoring with split-bandwidth interferometry: A case study of the shuping landslide in the three Gorges area," *Remote Sens.*, vol. 9, no. 9, 2017, Art. no. 937.

[55] S. Vitousek, P. L. Barnard, C. H. Fletcher, N. Frazer, L. Erikson, and C. D. Storlazzi, "Doubling of coastal flooding frequency within decades due to sea-level rise," *Sci. Rep.*, vol. 7, no. 1, 2017, Art. no. 1399.
[56] A. Cazenave and G. L. Cozannet, "Sea level rise and its coastal impacts," *Earth's Future*, vol. 2, no. 2, pp. 15–34, 2014.
[57] E. E. Lentz, E. R. Thieler, N. G. Plant, S. R. Stippa, R. M. Horton, and D. B. Gesch, "Evaluation of dynamic coastal response to sea-level rise modifies inundation likelihood," *Nature Climate Change*, vol. 6, no. 7, pp. 696–700, 2016.
[58] P. Gong *et al.*, "Stable classification with limited sample: Transferring a 30-m resolution sample set collected in 2015 to mapping 10-m resolution global land cover in 2017," *Sci. Bull.*, vol. 64, no. 6, pp. 370–373, 2019.
[59] K. Zhang, D. Gann, M. Ross, H. Biswas, Y. Li, and J. Rhome, "Comparison of TanDEM-X DEM with LiDAR data for accuracy assessment in a coastal urban area," *Remote Sens.*, vol. 11, no. 7, 2019, Art. no. 876.
[60] D. Massonnet and K. L. Feigl, "Radar interferometry and its application to changes in the earth's surface," *Rev. Geophys.*, vol. 36, no. 4, pp. 441–500, 1998.
[61] R. F. Hanssen, *Radar Interferometry: Data Interpretation and Error Analysis*. Dordrecht, the Netherlands: Kluwer Academic Publishers, 2001.
[62] J. Biggs, T. Wright, Z. Lu, and B. Parsons, "Multi-interferogram method for measuring interseismic deformation: Denali fault, Alaska," *Geophys. J. Int.*, vol. 170, no. 3, pp. 1165–1179, 2007.
[63] A. Ferretti, C. Prati, and F. Rocca, "Permanent scatterers in SAR interferometry," *IEEE Trans. Geosci. Remote Sens.*, vol. 39, no. 1, pp. 8–20, Jan. 2001.
[64] P. Berardino, G. Fornaro, R. Lanari, and E. Sansosti, "A new algorithm for surface deformation monitoring based on small baseline differential SAR interferograms," *IEEE Trans. Geosci. Remote Sens.*, vol. 40, no. 11, pp. 2375–2383, Nov. 2002.
[65] Z. H. Li, E. J. Fielding, and P. Cross, "Integration of InSAR time-series analysis and water-vapor correction for mapping postseismic motion after the 2003 Bam (Iran) earthquake," *IEEE Trans. Geosci. Remote Sens.*, vol. 47, no. 9, pp. 3220–3230, Sep. 2009.
[66] H. Fattahi and F. Amelung, "DEM error correction in InSAR time series," *IEEE Trans. Geosci. Remote Sens.*, vol. 51, no. 7, pp. 4249–4259, Jul. 2013.
[67] K. R. Koch, *Parameter Estimation and Hypothesis Testing in Linear Models*, 2nd ed. Berlin, Germany: Springer-Verlag, 1999.
[68] B. Bayer, D. Schmidt, and A. Simoni, "The influence of external digital elevation models on PS-InSAR and SBAS results: Implications for the analysis of deformation signals caused by slow moving landslides in the northern Apennines (Italy)," *IEEE Trans. Geosci. Remote Sens.*, vol. 55, no. 5, pp. 2618–2631, May 2017.

**Peng Li** received the B.Sc. degree in geodesy from the Changchun Institute of Technology, Changchun, China, in 2007, and the Ph.D. degree in geodesy and geomatics from the Wuhan University, Wuhan, China, in 2013.

He was a Visiting Ph.D. Student with the University of Glasgow, Glasgow, U.K., in 2012, and a Postdoctoral Research Fellow with the Ocean University of China, Qingdao, China, from 2016 to 2019, and an Academic Visitor with the Newcastle University, Newcastle upon Tyne, U.K., in 2019. Since 2015, he has been a Lecturer of coastal remote sensing with the Institute of Estuarine and Coastal Zone, College of Marine Geosciences, Ocean University of China. His research interests include radar interferometry, coastal DEM, deformation, and land cover mapping.

**Zhenhong Li** (Senior Member, IEEE) received the B.Sc. degree in geodesy from the Wuhan University, Wuhan, China, in 1997, and the Ph.D. degree in GPS, geodesy, and navigation from the University College London, London, U.K., in 2005.

He was the Professor of imaging geodesy, from 2014 to 2020, with the School of Engineering, Newcastle University, Newcastle upon Tyne, U.K. He is currently a Professor and Dean with the College of Geological Engineering and Geomatics, Chang'an University, Xi'an, China, and a Guest Professor with the College of Marine Geoscience, Ocean University of China, Qingdao, China. He has more than 20 years of research experience in space geodesy and remote sensing [mainly synthetic aperture radar interferometry (InSAR) and Global Navigation Satellite System] and their application to geohazards (e.g., earthquakes, landslides, and land subsidence) and precision agriculture. He is a Principal Investigator with the Generic Atmospheric Correction Online Service for InSAR. His research interests include development of InSAR atmospheric corrections and time-series algorithms for precisely mapping surface movements, and he has made several original contributions to the direct estimation and/or mitigation of the effects of atmospheric water vapor on satellite radar measurements.

Prof. Li is a Fellow of the International Association of Geodesy and an Associate Editor of *Advances in Space Research and Remote Sensing*.

**Keren Dai** received the B.Eng. degree in remote sensing technology and application and the Ph.D. degree in photogrammetry and remote sensing from Southwest Jiaotong University, Chengdu, China, in 2012 and 2017, respectively.

He was a Visiting Ph.D. Student with Newcastle University, Newcastle upon Tyne, U.K., from 2014 to 2015, and has been a Postdoctoral Researcher with Chang'an University, Xi'an, China, since 2019. He is currently a Professor with the College of Earth Science, Chengdu University of Technology, Chengdu, China, as well as a Research Scientist with the State Key Laboratory of Geohazard Prevention and Geoenvironment Protection. His research interests include landslide detection, mapping, and monitoring with interferometric synthetic aperture radar and multispectral remote sensing.

Prof. Dai was the recipient of the Promising Young Scientist Award by the International Consortium on Geodisaster Reduction, in 2017.

**Yasir Al-Husseinawi** received the Ph.D. degree in photogrammetry and remote sensing from the Newcastle University, Newcastle upon Tyne, U.K., in 2019.

He is currently a Consultant with the Ministry of water resources, Department of State commission of survey, Iraq. His interests include radar interferometry and geological disasters.

**Wanpeng Feng** received the B.Sc. degree in geological engineering from China University of Mining and Technology, Beijing, China, in 2003, and the Ph.D. degree in earth sciences from the University of Glasgow, Glasgow, U.K., in 2015.

He worked as a Research Scientist with Canada Center of Mapping and Earth Observation, from 2016 to 2018. Since then, he has been an Associate Professor with the School of Earth Science and Engineering, Sun Yat-sen University, Zhuhai, China. His research interests include geophysical inversion and development of InSAR deformation mapping techniques.

Dr. Feng was the recipient of the NSERC Visiting Fellowship based on CCMEO and NRACan from 2015 to 2016.

**Houjie Wang** received the B.Sc. degree in coastal engineering and the Ph.D. degree in marine geology from Ocean University of China, Qingdao, China, in 1996 and 2002, respectively.

He was an Academic Visitor with the University of New South Wales, Sydney, NSW, Australia, in 2008, and the North Carolina State University, Raleigh, NC, USA, in 2006. He is currently a Professor and Dean with the College of Marine Geoscience, Ocean University of China, Qingdao, China. His research interests include earth observation and global change, coastal, and river delta vulnerability.

Prof. Wang has been supported by the National Science Foundation for Distinguished Young Scholars of China, since 2015.